The FEBS Journal

FEBS PRESS science publishing by scientists

Reverse protein engineering of a novel 4-domain copper nitrite reductase reveals functional regulation by protein–protein interaction

Daisuke Sasaki[1], Tatiana F. Watanabe[1,2], Robert R. Eady[1], Richard C. Garratt[2], Svetlana V. Antonyuk[1] and S. Samar Hasnain[1]

1 Molecular Biophysics Group, Institute of Systems, Molecular and Integrative Biology, Faculty of Health and Life Sciences, University of Liverpool, UK

2 The São Carlos Institute of Physics,University of São Paulo, São Carlos, Brazil

Keywords

catalysis; denitrification; electron transfer; multidomain protein; protein engineering

Correspondence

S. S. Hasnain, Molecular Biophysics Group, Faculty of Health and Life Sciences, Institute of Integrative Biology, University of Liverpool, UK

Tel: +44 151 795 5149

E-mail: s.s.hasnain@liverpool.ac.uk

website: http://www.biophysics.liv.ac.uk/

(Received 16 December 2019, revised 16 March 2020, accepted 1 April 2020)

doi:10.1111/febs.15324

Cu-containing nitrite reductases that convert NO_2^- to NO are critical enzymes in nitrogen-based energy metabolism. Among organisms in the order *Rhizobiales*, we have identified two copies of *nirK*, one encoding a new class of 4-domain CuNiR that has both cytochrome and cupredoxin domains fused at the N terminus and the other, a classical 2-domain CuNiR (Br^{2D}NiR). We report the first enzymatic studies of a novel 4-domain CuNiR from *Bradyrhizobium* sp. ORS 375 (*Br*NiR), its genetically engineered 3- and 2-domain variants, and Br^{2D}NiR revealing up to ~ 500-fold difference in catalytic efficiency in comparison with classical 2-domain CuNiRs. Contrary to the expectation that tethering would enhance electron delivery by restricting the conformational search by having a self-contained donor–acceptor system, we demonstrate that 4-domain *Br*NiR utilizes N-terminal tethering for downregulating enzymatic activity instead. Both Br^{2D}NiR and an engineered 2-domain variant of *Br*NiR (Δ(Cyt*c*-Cup) *Br*NiR) have 3 to 5% NiR activity compared to the well-characterized 2-domain CuNiRs from *Alcaligenes xylosoxidans* (*Ax*NiR) and *Achromobacter cycloclastes* (*Ac*NiR). Structural comparison of Δ(Cyt*c*-Cup) *Br*NiR and Br^{2D}NiR with classical 2-domain *Ax*NiR and *Ac*NiR reveals structural differences of the proton transfer pathway that could be responsible for the lowering of activity. Our study provides insights into unique structural and functional characteristics of naturally occurring 4-domain CuNiR and its engineered 3- and 2-domain variants. The reverse protein engineering approach utilized here has shed light onto the broader question of the evolution of transient encounter complexes and tethered electron transfer complexes.

Enzyme

Copper-containing nitrite reductase (CuNiR) (EC 1.7.2.1).

Database

The atomic coordinate and structure factor of Δ(Cyt*c*-Cup) *Br*NiR and Br^{2D}NiR have been deposited in the Protein Data Bank (http://www.rcsb.org/) under the accession code 6THE and 6THF, respectively.

Abbreviations

DEAE, diethylaminoethyl; ET, electron transfer; LB, Luria–Bertani; NOS, nitric oxide synthase; OD, optical density; PDB, Protein Data Bank; SEC, size exclusion chromatography; TEV, tobacco etch virus; UV, ultraviolet.

Introduction

Protein–protein complexes and associated electron transfer (ET) reactions are essential to life since they underpin photosynthesis and respiratory processes leading to the generation of ATP [1]. Additionally, an abundance of genomic data and advanced proteomic approaches has identified numerous protein complexes and their importance in metabolic networks [2]. Despite their central role, our understanding of how the structure and function of an enzyme containing a core catalytic domain may be altered and regulated through interactions with cognate partner protein(s) remains limited. This limitation is a consequence of the transient nature of these protein complexes that requires coaxing of component proteins to form stable complexes so that they become amenable to biophysical studies.

Copper-containing nitrite reductases, encoded by *nirK*, are involved in the denitrification branch of the global nitrogen cycle where nitrate is used in place of dioxygen as an electron acceptor in respiratory energy metabolism [3]. An additional role is in nitrification, the aerobic oxidative conversion of ammonium to nitrate via nitrite. Both processes are of environmental importance since they result in the release into the atmosphere of NO and N_2O, contributing to depletion of the ozone layer with N_2O being the third most significant greenhouse gas with a 300 times global warming potential of CO_2 [4]. CuNiRs found in fungi, bacteria, and archaea that are widely distributed in marine and terrestrial environments suggest an early evolutionary origin [5]. They catalyze the one-electron reduction of nitrite $[NO_2^- + e^- + 2H^+ \rightleftarrows NO + H_2O]$. This is a key reaction in denitrification since it is at this point that bioavailable fixed nitrogen is lost to the atmosphere. NO is subsequently reduced by nitric oxide reductase to form nitrous oxide N_2O.

The structures of the well-characterized homotrimeric 2-domain enzymes (subsequently referred to as 2D-CuNiR) are highly conserved. The catalytic type 2 Cu center (T2Cu) is located at the interface of two adjacent monomers and linked to the electron donating T1Cu center *via* a Cys-His bridge. The T1Cu center is positioned near the protein surface and has been shown to function as an electron acceptor from the physiological periplasmic electron donors azurin, pseudoazurin [6], or cytochrome [7], depending on the species. Two invariant active-site pocket residues Asp_{CAT} and His_{CAT} are involved in substrate binding and catalysis [8–13].

In addition to the well-studied 2D-CuNiRs, three new classes of CuNiR have been identified with an additional domain where either a c-type heme or a T1Cu center is tethered to the core of the 2-domain CuNiR at the C or N/C terminus (Fig. 1A) [14–16]. Genome analyses revealed that 30% of *nirK*-dependent denitrifiers [4,17] have a 3-domain CuNiR, suggesting it plays an important role in the nitrogen cycle. However, only single representative of the N-terminal (*Hyphomicrobium denitrificans* strain A3151 (*Hd*NiR)) [14] and C-terminal (*Thermus scotoductus* (*Ts*NiR)) [16], cupredoxin-extended enzymes and two of the C-terminal heme-extended enzymes from *Ralstonia pickettii* (*Rp*NiR) [15], and *Pseudoalteromonas haloplanktis* (*Ph*NiR) [18] have been biochemically and structurally characterized. Despite the self-containment of the redox partner in these tethered systems, the NiR catalytic activity, that is, conversion of NO_2^- to NO, is significantly lower compared to the 2D-CuNiRs.

Here, we provide the first identification and isolation of a novel 4-domain CuNiR from *Bradyrhizobium* sp. ORS 375 (*Br*NiR) that has both cytochrome and cupredoxin domains fused at the N terminus. We used reverse protein engineering to construct an N-terminal tethered 3-domain version, equivalent to *Hd*NiR and also the 2-domain core enzyme, equivalent to well-studied 2D-CuNiRs from *Alcaligenes xylosoxidans* (*Ax*) and *Achromobacter cycloclastes* (*Ac*). This allowed us to demonstrate that the presence of the cupredoxin and heme domains downregulates the activity of *Br*NiR with the highest activity observed for the core 2D enzyme. These data show that tethering does not always provide a higher catalysis from domain interaction as has been previously suggested for NOS [19] and cytochrome P-450 BM3 [20]. Our data lend support to the concept that tethering does not enhance the rate of electron delivery from its tethered redox partner to the catalytic copper-containing core but tethering communicates the redox status of the partner to the distant T2Cu center that helps initiate substrate binding for catalysis [21]. Tethering may also be used by Nature to downregulate the activity of the core enzyme. Br^{2D}NiR, despite a 70% conservation in the primary structure and similarity of crystallographic structure, revealed a 20-fold lower activity than *Ax*NiR and *Ac*NiR, suggesting subtle changes are introduced by natural pressures to respond to differing denitrification requirements of an organism and its habitat.

Results and Discussion

Discovery of a novel 4-domain CuNiR in *Rhizobiales*

We report the discovery of a new class of 4-domain heme-cupredoxin CuNiR in several α-proteobacteria of

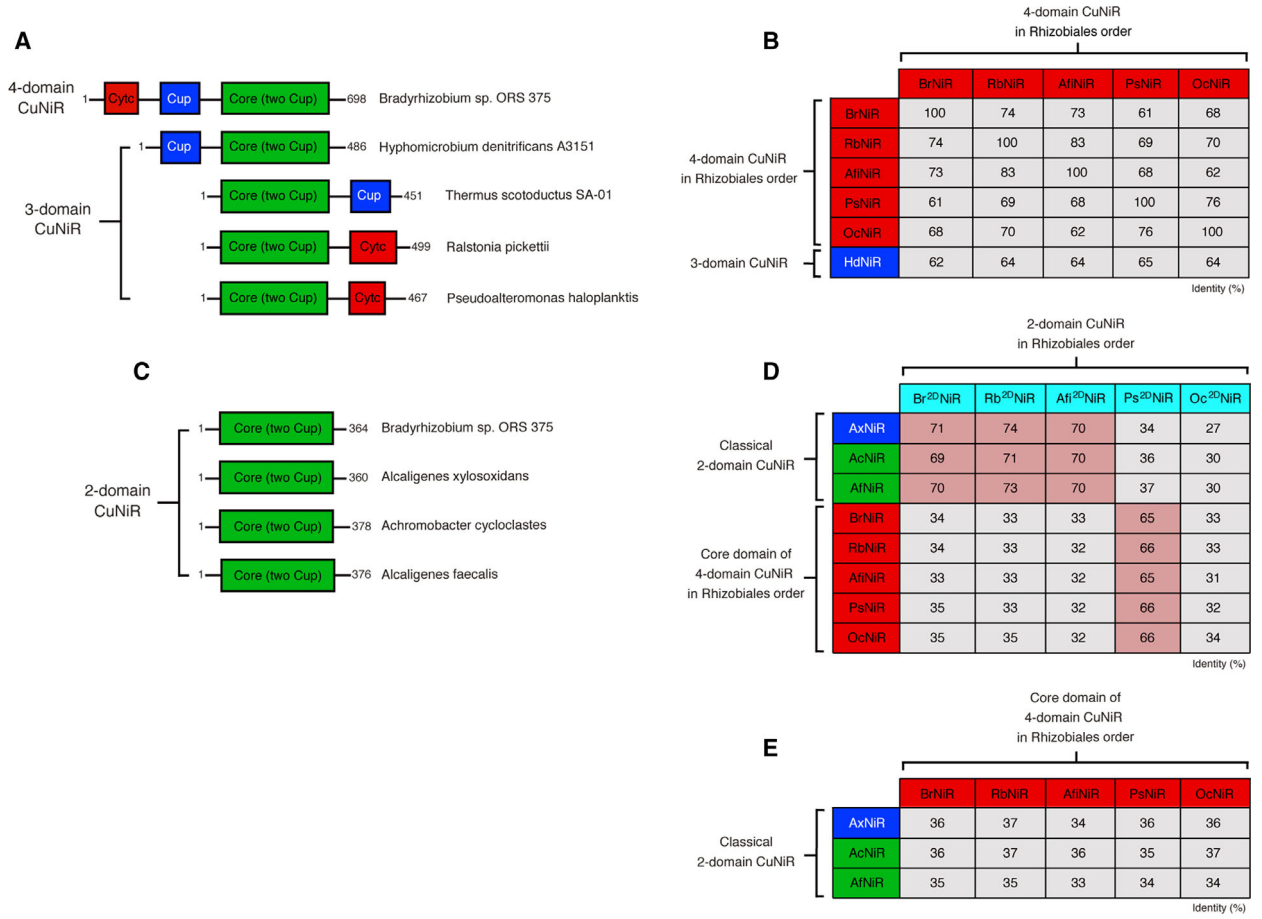

Fig. 1. Distinct domain architectures of CuNiRs. (A) Domain architectures of 3- and 4-domain CuNiRs. Cytochrome *c* (Cyt*c*) domain, extra cupredoxin (Cup) domain, and the two Cup domains (Core) are colored in red, blue, and green, respectively, and number of amino-acid residues is indicated. (B) Amino acid sequence identity matrix between 4-domain CuNiRs in *Rhizobiales* order and 4-domain CuNiRs in *Rhizobiales* order/3-domain *Hd*NiR. The 4-domain CuNiRs from *Bradyrhizobium* sp. ORS 375 (*Br*NiR; UniProt: H0SHH5), *Rhizobiales bacterium* 62-47 (*Rb*NiR; UniProt: A0A1Q4BYF3), *Afipia* sp. 1NLS2 (*Afi*NiR; UniProt: D6V7F6), *Pseudolabrys* sp. Root1462 (*Ps*NiR; UniProt: A0A0Q7TQS6), *Oligotropha carboxidovorans* ATCC 49405 (*Oc*NiR; UniProt: B6JIX6), and the 3-domain CuNiR from *Hyphomicrobium denitrificans* strain A3151 (*Hd*NiR; UniProt: Q8KKH4) are shown. (C) Domain architectures of 2-domain CuNiRs. The two Cup domains (Core) are colored in green, and number of amino-acid residues is indicated. (D) Amino acid sequence identity matrix between 2-domain CuNiRs in *Rhizobiales* order and classical 2-domain CuNiRs/core domains of 4-domain CuNiR in the same organisms. High and low identity are highlighted in red and grey, respectively. The 2-domain CuNiRs from *Bradyrhizobium* sp. ORS 375 (Br^{2D}NiR; UniProt: H0SLX7), *Rhizobiales bacterium* 62-47 (Rb^{2D}NiR; UniProt: A0A1Q4BUR6), *Afipia* sp. 1NLS2 (Afi^{2D}NiR; UniProt: D6V3F0), *Pseudolabrys* sp. Root1462 (Ps^{2D}NiR; UniProt: A0A0Q7U0E7), *Oligotropha carboxidovorans* ATCC 49405 (Oc^{2D}NiR; UniProt: F8BSH2), *Alcaligenes xylosoxidans* (*Ax*NiR; UniProt: O68601), *Achromobacter cycloclastes* (*Ac*NiR; UniProt: P2506), and *Alcaligenes faecalis* (*Af*NiR; UniProt: P38501) are shown. (E) Amino acid sequence identity matrix between core domains of 4-domain CuNiR in *Rhizobiales* order and classical 2-domain CuNiRs.

the order *Rhizobiales*. Their primary structures reveal a 2-domain CuNiR core to which both a cytochrome *c* and a cupredoxin domain are tethered at the N terminus (Fig. 1A). We report the first characterization of a 4-domain CuNiR, the recombinant enzyme from *Bradyrhizobium* sp. ORS 375 (*Br*NiR). This photosynthetic nitrogen-fixing organism unusually, but specifically, forms stem nodules with some leguminous species of the genus *Aeschynomene* [22]. In addition to *Bradyrhizobium* sp. ORS 375, the *nirK* gene encoding the new 4-domain CuNiRs was found in several members of the order *Rhizobiales* including *Rhizobiales bacterium* 62-47 (*Rb*NiR), *Afipia* sp. 1NLS2 (*Afi*NiR), *Pseudolabrys* sp. Root1462 (*Ps*NiR), and *Oligotropha carboxidovorans* ATCC 49405 (*Os*NiR).

The multiple amino acid sequence alignment shows that these 4-domain CuNiRs are highly conserved among the different organisms analyzed, with the

sequence identity ranging from 61% to 83% (Fig. 1B), and also have over 60% sequence identity with the only N-terminal tethered 3-domain CuNiR, *Hd*NiR (Fig. 1B). Phylogenetic studies of *nirK* have shown the existence of two distinct clades of CuNiRs, with both classes of 3-domain enzymes grouped in Clade 2, which contains a taxonomically diverse range of denitrifiers. They are characterized by the sequence $SSFH_{CAT}V(L)$ around the essential His active-site residue (His_{CAT}) as we also found for all of the 4-domain CuNiRs (Figs 2A and 3). The Clade 1 group that includes the classical 2-domain enzymes *Ax*NiR, *Ac*NiR, and *Af*NiR has the sequence $TRPH_{CAT}L$ (Figs 2B and 3).

These *Rhizobiales* also have an additional copy of the *nirK* gene (only five percent of CuNiR denitrifiers have two or more copies of *nirK,* with *Rhizobiales* being the only order shown to have 4-domain CuNiR.), which encodes a 2-domain CuNiR, referred to for clarity as Br^{2D}NiR (Fig. 1C). This is the first example of the coexistence of the CuNiRs with distinct 4- and 2-domain architecture in the same organism. There is a sequence divergence in these enzymes except for Ps^{2D}NiR when compared with the corresponding 4-domain CuNiR core from the same organism (Fig. 1D) as well as in the classical 2-domain enzymes *Ax*NiR, *Ac*NiR, and *Af*NiR when compared with the 4-domain enzyme core (Fig. 1E). In contrast, the 2-domain enzymes from *Bradyrhizobium* sp. ORS 375, *Rhizobiales bacterium* 62-47, and *Afipia* sp. 1NLS2 have a sequence identity of ~ 70% with the classical 2-domain enzymes *Ax*NiR, *Ac*NiR, and *Af*NiR compared with ~ 30% identity to the core domain of the corresponding 4-domain enzymes. They have a $S(T)RPH_{CAT}L$ sequence at the active site (Fig. 2B) placing them in Clade 1, rather than Clade 2, of the corresponding 4-domain enzymes. The sequence of Ps^{2D}NiR suggests it should be classified within Clade 2, consistent with its active-site sequence (Fig. 2B). Together with Oc^{2D}NiR, which shows poor sequence identity with both clades, this implies a complex history of evolutionary events within the family involving gene duplications, fusions, and deletions, presumably as adaptive responses to selective pressure.

Nitrite reductase activities of the 4-domain and the 2-domain CuNiR of *Bradyrhizobium*

The nitrite reductase activity of the 4-domain *Br*NiR is fourfold lower than Br^{2D}NiR (Table 1). The multiple copies of *nir*K in *Rhizobiales* with different activities may offer particular advantages in response to bioavailability of nitrite in differing habitats and/or other environmental pressures. The involvement of *nir*K in anaerobic ammonium oxidation [23] and nitrifier denitrification [24] pathways also provides potential for the retention of multiple gene copies. An alternate possibility is that these enzymes have dual enzymatic functions; for example, it has been shown that the reduction of toxic selenite to elemental selenium in a strain of *Rhizobium* isolated from soils with a high selenite concentration is *nirK* dependent [25]. The activity of Br^{2D}NiR is ~ 20-fold lower than two of the best-studied 2-domain CuNiRs representing the blue (*Ax*NiR) and green (*Ac*NiR) subclasses of two-domain CuNiRs (Table 1). To understand this further, we determined the structure of Br^{2D}NiR (see below).

The multiple amino acid sequence alignment of 4-domain *Br*NiR with well-studied 2D-CuNiRs shows complete conservation of the residues ligated to the T1Cu and T2Cu centers, and also, the Asp_{CAT}/His_{CAT} residues around the T2Cu involved in substrate binding and catalysis (Fig. 3). Extensive structural, computational, and biophysical studies of 2-domain CuNiRs have shown that Asp_{CAT} in the catalytic pocket plays an essential role in catalysis participating in proton transfer to nitrite bound to the T2Cu ion [11,13,26,27]. Mutation of this residue in *Ax*NiR and *Af*NiR results in loss of > 95% of activity [13]. To investigate the nature of the catalytic core of *Br*NiR, we made a mutation of Asp_{CAT} by constructing the D439N variant (Fig. 3). This substitution resulted in a ~ 97% loss of activity (Table 1) demonstrating the preservation of the catalytic core of CuNiRs in *Br*NiR and the importance of this residue in catalysis.

Properties of synthetically deconstructed *Br*NiR variants

In order to investigate the potential role of the additional tethered domains in modulating the NiR activity of *Br*NiR, we used a reverse protein engineering approach to deconstruct the wild-type enzyme into a 3-domain (cupredoxin-fused) and 2-domain (core) CuNiRs. To guide this process, amino acid sequence alignment based on domain sequence conservation was utilized. Removal of the heme domain gave a construct, Δ*Cytc Br*NiR, with a similar domain organization to the 3-domain *Hd*NiR. Removal of both heme and cupredoxin domains generated a core 2-domain enzyme, Δ(Cyt*c*-Cup) *Br*NiR, with a similar domain organization to *Ax*NiR, *Ac*NiR, *Af*NiR, and Br^{2D}NiR. The alignment of Δ*Cytc Br*NiR with *Hd*NiR shows an equivalent sequence length with high sequence identity of ~ 60% (Fig. 4A), whereas Δ(Cyt*c*-Cup) *Br*NiR shows only ~ 35% sequence identity with *Ax*NiR,

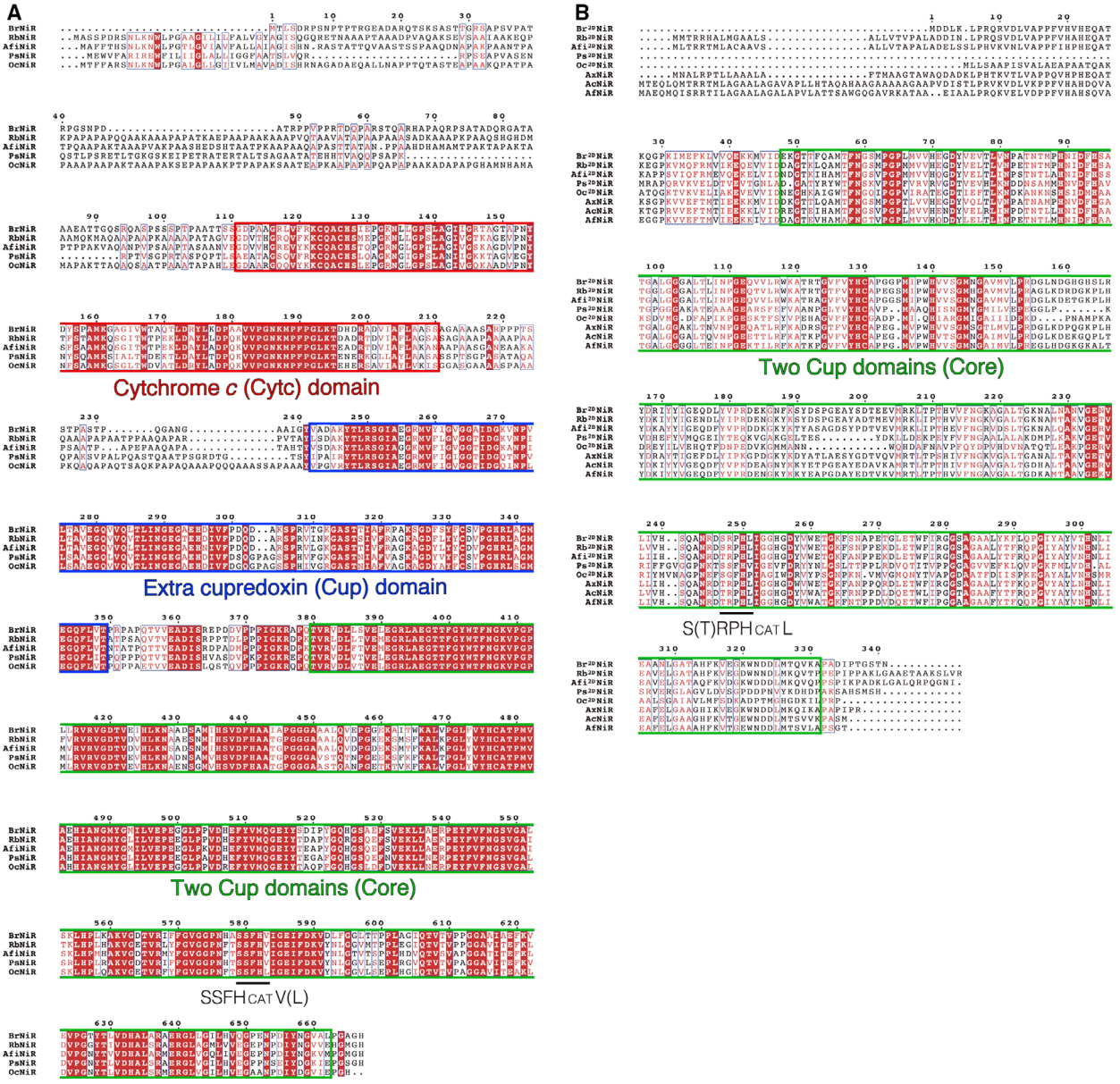

Fig. 2. Multiple amino acid sequence alignment among 4- and 2-domain CuNiRs in *Rhizobiales* order. (A) The 4-domain CuNiRs from *Bradyrhizobium* sp. ORS 375 (*Br*NiR; UniProt: H0SHH5), *Rhizobiales bacterium* 62-47 (*Rb*NiR; UniProt: A0A1Q4BYF3), *Afipia* sp. 1NLS2 (*Afi*NiR; UniProt: D6V7F6), *Pseudolabrys* sp. Root1462 (*Ps*NiR; UniProt: A0A0Q7TQS6), and *Oligotropha carboxidovorans* ATCC 49405 (*Oc*NiR; UniProt: B6JIX6) are aligned. The cytochrome *c* domain (Cyt*c*), extra cupredoxin domain (Cup), and the two Cup domains (Core) are shown in red, blue, and green boxes, respectively. The $SSFH_{CAT}V(L)$ sequence is indicated. Numbering is for *Br*NiR without N-terminal signal peptide. (B) The 2-domain CuNiRs from *Bradyrhizobium* sp. ORS 375 (Br^{2D}NiR; UniProt: H0SLX7), *Rhizobiales bacterium* 62-47 (Rb^{2D}NiR; UniProt: A0A1Q4BUR6), *Afipia* sp. 1NLS2 (Afi^{2D}NiR; UniProt: D6V3F0), *Pseudolabrys* sp. Root1462 (Ps^{2D}NiR; UniProt: A0A0Q7U0E7), *Oligotropha carboxidovorans* ATCC 49405 (Oc^{2D}NiR; UniProt: F8BSH2), *Alcaligenes xylosoxidans* (*Ax*NiR; UniProt: O68601), *Achromobacter cycloclastes* (*Ac*NiR; UniProt: P2506), and *Alcaligenes faecalis* (*Af*NiR; UniProt: P38501) are aligned. The two Cup domains (Core) are shown in green box. The $S(T)RPH_{CAT}L$ sequence is indicated. Numbering is for Br^{2D}NiR without N-terminal signal peptide. Identical amino acids are highlighted by white letters in red boxes, and similar ones are shown by red letter in white boxes. Multiple sequence alignment was performed with ClustalW [34], and the aligned sequences were illustrated using ESPript [35].

*Ac*NiR, *Af*NiR, and Br^{2D}NiR (Fig. 4B). The weak sequence identity exhibited by the core enzyme Δ(Cyt*c*-Cup) *Br*NiR with a range of 2D-CuNiRs is similar to that of AniA, the CuNiR of pathogenic *Neisseria* [28]. The Δ(Cyt*c*-Cup) *Br*NiR shows higher ~ 52% sequence identity with AniA compared to the 2D-CuNiRs.

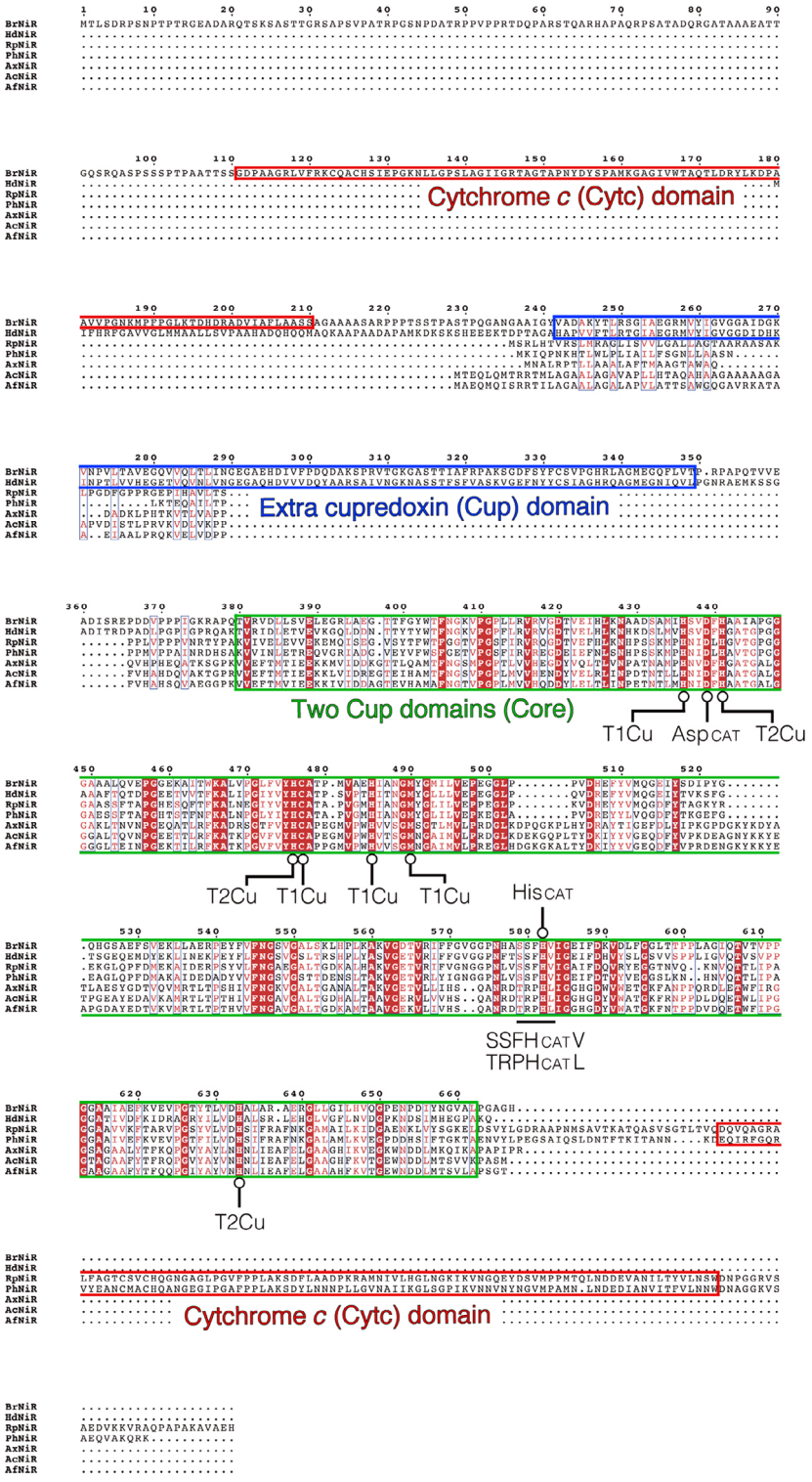

Fig. 3. Multiple amino acid sequence alignment among 2-, 3-, and 4-domain CuNiRs from different organisms shown in Fig. 1A,C. The 4-domain CuNiR from *Bradyrhizobium* sp. ORS 375 (*Br*NiR; UniProt: H0SHH5), 3-domain CuNiRs from *Hyphomicrobium denitrificans* strain A3151 (*Hd*NiR; UniProt: Q8KKH4)/*Ralstonia pickettii* (*Rp*NiR; UniProt: I6NAW4)/*Pseudoalteromonas haloplanktis* (*Ph*NiR; UniProt: Q3IGF7), and 2-domain CuNiRs from *Alcaligenes xylosoxidans* (*Ax*NiR; UniProt: O68601)/*Achromobacter cycloclastes* (*Ac*NiR; UniProt: P25006)/*Alcaligenes faecalis* (*Af*NiR; UniProt: P38501) are aligned. The cytochrome *c* domain (Cyt*c*), extra cupredoxin domain (Cup), and the two Cup domains (Core) are shown in red, blue, and green boxes, respectively. The completely conserved residues ligated to the T1Cu and T2Cu centers and the Asp_{CAT}/His_{CAT} residues around the T2Cu, which are involved in substrate binding and catalysis, are indicated. The $SSFH_{CAT}V(L)/S(T)RPH_{CAT}L$ sequence is indicated. Numbering is for *Br*NiR without N-terminal signal peptide. Identical amino acids are highlighted by white letters in red boxes, and similar ones are shown by red letter in white boxes. Multiple sequence alignment was performed with ClustalW [34], and the aligned sequences were illustrated using ESPript [35].

The UV-visible absorption spectra of *Br*NiR are dominated by the contribution of the *c*-heme that masks the T1Cu absorption bands of the core and additional N-terminal cupredoxin domain. The availability of the deconstructed ΔCyt*c* and Δ(Cyt*c*-Cup) engineered *Br*NiR enzymes allowed us to define spectral properties of the oxidized and reduced derivatives of the additional cytochrome (Fig. 5A), extra

Table 1. Distinct domain architecture and specific NiR activity of CuNiRs.

Enzyme	Domain(s)[a]	Specific activity[b] [nmol s^{-1} (nmol of protein)$^{-1}$]
WT *Br*NiR	Cyt*c*-Cup-Core	9.38 ± 0.29
D439N *Br*NiR	Cyt*c*-Cup-Core	0.08 ± 0.00
ΔCyt*c* *Br*NiR[c]	Cup-Core	1.67 ± 0.13
*Hd*NiR	Cup-Core	67.8 ± 5.5
Δ(Cyt*c*-Cup) *Br*NiR[d]	Core	27.9 ± 3.3
Br^{2D}NiR	Core	40.5 ± 1.6
*Ax*NiR	Core	888.4 ± 20.3
*Ac*NiR	Core	923.8 ± 15.1

[a]Cyt*c*: cytochrome *c* domain, Cup: (extra) cupredoxin domain, Core: two cupredoxin domains.
[b]Errors are estimated from 3 independent measurements.
[c]Cytochrome *c* domain-truncated mutant of 4-domain WT *Br*NiR.
[d]Cytochrome *c*/extra cupredoxin domains-truncated mutant of 4-domain WT *Br*NiR.

cupredoxin (Fig. 5B), and core (Fig. 5C) domains. In terms of the absorbance ratio A_{600}/A_{460}, the profile of ΔCyt*c* (~ 1.6) is more greenish than *Hd*NiR (~ 2.9) (Fig. 5B) and that of Δ(Cyt*c*-Cup) (~ 0.9) is more similar to green *Ac*NiR (~ 0.7) than blue *Ax*NiR (~ 3.3) (Fig. 5C). The significant difference between ΔCyt*c* (~ 1.6) and Δ(Cyt*c*-Cup) (~ 0.9) due to removal of the extra cupredoxin domain is consistent with the spectral profile in *Hd*NiR from the native source and its core domain fragment [29].

The size exclusion chromatography profiles of WT and ΔCyt*c* *Br*NiRs showed a trimer/hexamer mixture with the trimer as the major species (Figs 6A,B). The WT profile showed a higher hexamer species that decreased on removal of the cyt domain in ΔCyt*c* *Br*NiR, to favor trimer formation. The core domain Δ(Cyt*c*-Cup) *Br*NiR showed a monomer/dimer mixture with the monomer predominating (Fig. 6C). These data are consistent with a role for the extra cupredoxin domain in hexamer formation as has been reported for *Hd*NiR [14]. Dissociation of the core enzyme to form a monomer seen in Δ(Cyt*c*-Cup) *Br*NiR has not been reported for any 2D-CuNiRs.

The activity assay profiles demonstrate that WT *Br*NiR and both ΔCyt*c* *Br*NiR and Δ(Cyt*c*-Cup) *Br*NiR were competent in reducing nitrite to NO (Fig. 7). Removal of cytochrome domain on its own decreases the nitrite reductase activity by ~ 6-fold, clearly demonstrating that the N-terminal tethering of cytochrome upregulates activity of ΔCyt*c* *Br*NiR (Table 1). On the other hand, the removal of both tethered domains increased the NiR activity by ~ 3-fold (Table 1), clearly demonstrating that the N-terminal tethering of cytochrome and extra cupredoxin downmodulates activity to the extent that *Br*NiR is ~ 100-fold less active than the classical 2-domain *Ax*NiR and *Ac*NiR (Table 1). Though the activity of 2D-CuNiR construct, Δ(Cyt*c*-Cup) *Br*NiR, increases compared to WT *Br*NiR, it is less than 4% of the classical 2-domain *Ax*NiR and *Ac*NiR (Table 1). To understand this further, the crystallographic structure of Δ(Cyt*c*-Cup) has been determined (see below). The activity of the ΔCyt*c* *Br*NiR was found to be much lower (~ 40-fold) than the structurally characterized *Hd*NiR [14], but both are less active than the classical 2-domain *Ax*NiR and *Ac*NiR (Table 1).

The time course for NO formation by the ΔCyt*c* *Br*NiR exhibited a significant lag period before the rate became linear when the reaction was initiated by the addition of enzyme to the assay mixture (Fig. 7B). The lag phase was eliminated when tethered extra cupredoxin domain was removed (Fig. 7B,C) or when ΔCyt*c* *Br*NiR was pre-incubated with reductant (ascorbate) before assay (Fig. 7B). These results suggest that the steady-state rate of turnover in the resting state of the intact enzyme is regulated by a slower event such as the conformational dynamics of the tethered cupredoxin domain in a manner similar to that recently been demonstrated for *Rp*NiR [21]. The observation that pre-incubation with electron donor overcomes the lag phase is consistent with a conformational equilibrium controlling access to the catalytic core and positioning of the ET centers. The active conformation is apparently stabilized by reduction of the Cu sites.

Structure of 2-domain Δ(Cyt*c*-Cup) *Br*NiR

We determined the crystallographic structure of Δ(Cyt*c*-Cup) *Br*NiR (Fig. 8A, Table 2). The overall architecture of the monomer is most similar to the core domain of 3-domain *Hd*NiR (PDB ID: 2DV6) [14] with an r.m.s.d. value of 0.76 (C-alphas). When compared with the classical 2-domain *Ax*NiR (PDB ID: 5ONY) [30], *Ac*NiR (PDB ID: 2BW4) [10], and *Af*NiR (PDB ID: 4YSE) [31], the C-alpha deviations were 1.74, 2.11 and 1.97Å, respectively, and when compared with Br^{2D}NiR (see below), C-alpha deviations were 1.90Å. Insight into the lower NiR activity of the catalytic core domain of 4-domain *Br*NiR, Δ(Cyt*c*-Cup) *Br*NiR, compared to classical 2-domain *Ax*NiR and *Ac*NiR (Table 1) is provided by closer examination of the crystallographic structures. The T1Cu-to-T2Cu ET pathway *via* a Cys125-His124 bridge is completely conserved, but significant differences are found in the major and minor proton pathways with the bridging waters almost missing in Δ(Cyt*c*-Cup) *Br*NiR (Fig. 8B), when compared to the

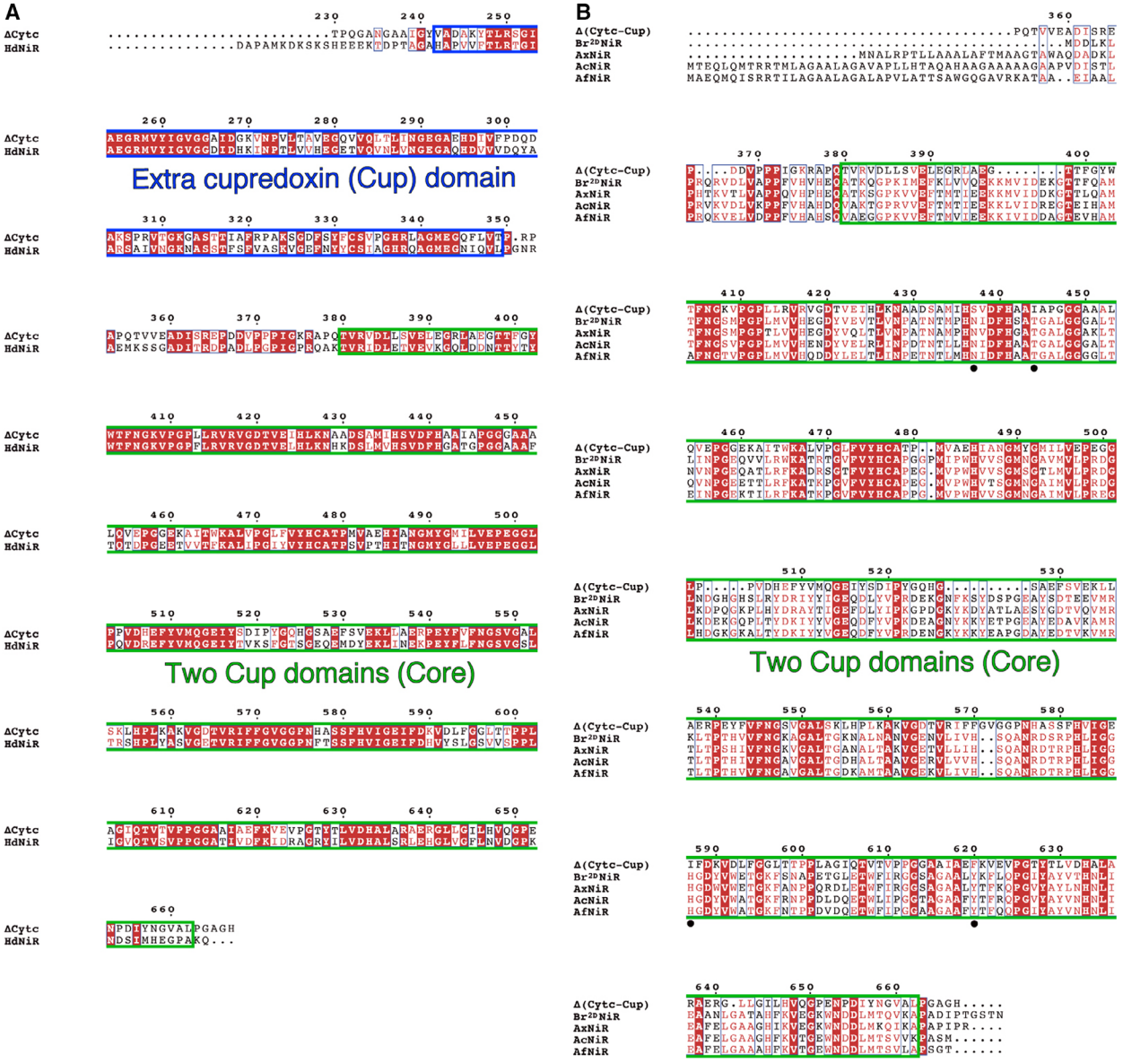

Fig. 4. Multiple amino acid sequence alignment between the cytochrome *c* domain-truncated mutant of 4-domain *Br*NiR and 3-domain CuNiRs and between the cytochrome *c*/extra cupredoxin domains-truncated mutant of 4-domain *Br*NiR and 2-domain CuNiRs. (A) The cytochrome *c* domain-truncated mutant ΔCyt*c* of 4-domain CuNiR from *Bradyrhizobium* sp. ORS 375 (*Br*NiR; UniProt: H0SHH5) and 3-domain CuNiR from *Hyphomicrobium denitrificans* strain A3151 (*Hd*NiR; UniProt: Q8KKH4) are aligned. The extra cupredoxin domain (Cup) and the two Cup domains (Core) are shown in blue and green boxes, respectively. Numbering is for ΔCyt*c*. (B) The cytochrome *c*/extra cupredoxin domains-truncated mutant Δ(Cyt*c*-Cup) of 4-domain CuNiR from *Bradyrhizobium* sp. ORS 375 (*Br*NiR; UniProt: H0SHH5) and 2-domain CuNiRs from *Bradyrhizobium* sp. ORS 375 (Br^{2D}NiR; UniProt: H0SLX7)/*Alcaligenes xylosoxidans* (*Ax*NiR; UniProt: O68601)/*Achromobacter cycloclastes* (*Ac*NiR; UniProt: P25006)/*Alcaligenes faecalis* (*Af*NiR; UniProt: P38501) are aligned. The two Cup domains (Core) are shown in green box. Difference amino acids observed in the major and minor proton pathways between Δ(Cyt*c*-Cup) and Br^{2D}NiR/*Ax*NiR/*Ac*NiR/*Af*NiR are shown by black closed circles. Numbering is for Δ(Cyt*c*-Cup). Identical amino acids are highlighted by white letters in red boxes, and similar ones are shown by red letter in white boxes. Multiple sequence alignment was performed with ClustalW [34], and the aligned sequences were illustrated using ESPript [35].

classical 2-domain *Ax*NiR and *Ac*NiR. The Asn90, which forms the entrance of the major proton pathway extending towards the $Asp92_{CAT}$/$His249_{CAT}$, is replaced by Ser85 (Figs 4B and 8B). This Asn-to-Ser substitution results in the difference in activity consistent with N90S *Ax*NiR mutant that has been shown to

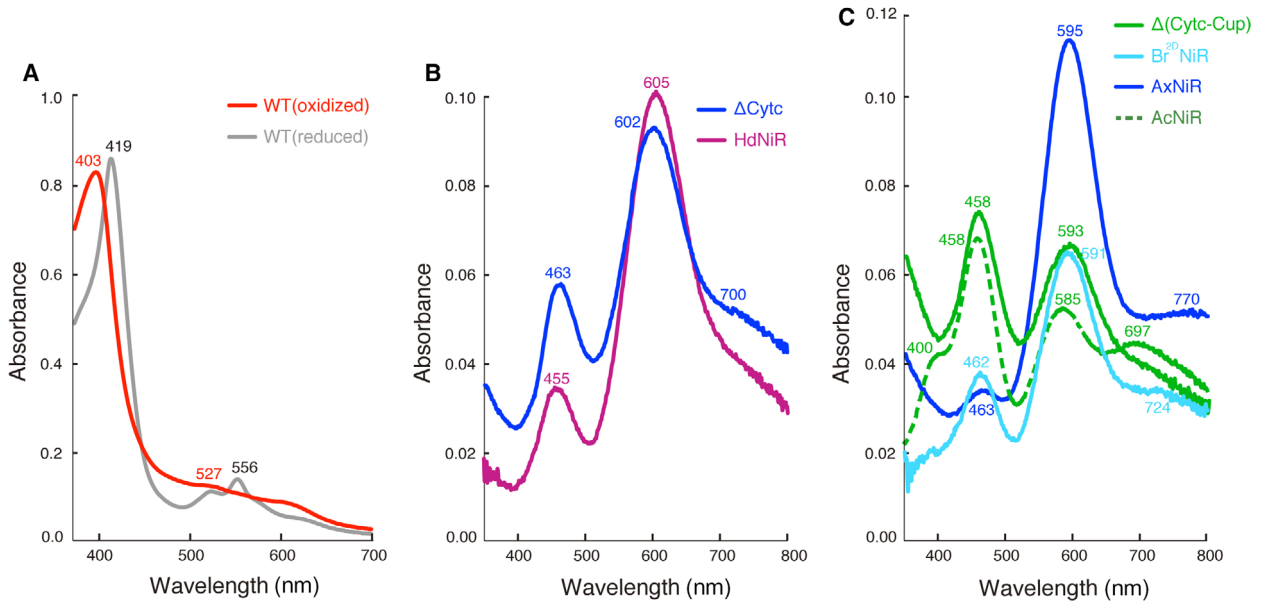

Fig. 5. Ultra violet-visible spectra profiles of the *Br*NiR variants and *Br*^{2D}NiR. Absorption profiles (absorption at 10 mm path vs wavelength [nm]) of (A) the oxidized wild-type *Br*NiR (WT) (red continuous line) and WT reduced with 100-fold molar excess of sodium dithionite (gray continuous line), (B) the oxidized cytochrome *c* domain-truncated mutant ΔCyt*c* (blue continuous line) and *Hd*NiR (purple continuous line), and (C) the oxidized cyt*c*/extra cupredoxin domains-truncated mutant Δ(Cyt*c*-Cup) (green continuous line), *Br*^{2D}NiR (cyan continuous line), *Ax*NiR (blue continuous line), and *Ac*NiR (green broken line) are shown. Values for the tops of absorption peaks are indicated.

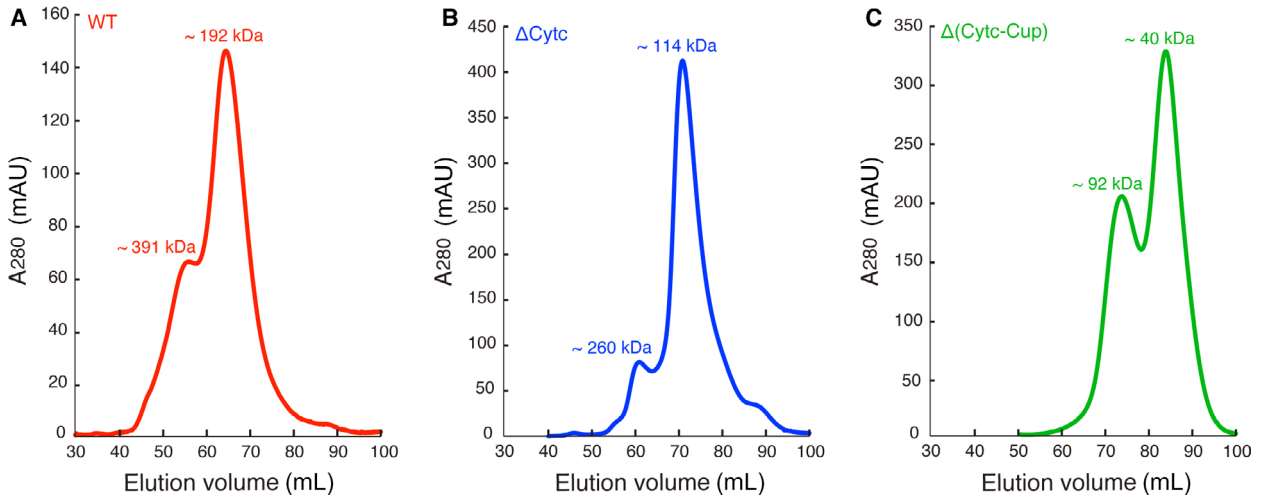

Fig. 6. The 2nd size exclusion chromatography (SEC) profiles of the *Br*NiR variants. Elution profiles (A_{280} [mAU] vs elution volume [mL]) of (A) the wild-type *Br*NiR (WT), (B) cyt*c* domain-truncated mutant ΔCyt*c*, and (C) cyt*c*/extra cupredoxin domains-truncated mutant Δ(Cyt*c*-Cup) are shown by red, blue, and green lines, respectively. Estimated molecular mass (kDa) is indicated. Theoretical molecular mass of a monomeric WT, ΔCyt*c*, and Δ(Cyt*c*-Cup) are of 70, 47, and 34 kDa, respectively.

decrease NiR activity by ~ 70% [32]. The His254, which is located at the gate between the entrance of the minor proton pathway and the $Asp92_{CAT}$/$His249_{CAT}$, is replaced by Ile235 (Figs 4B and 8B). In addition, the Thr97 and Tyr287, which form the entrance of the minor proton pathway, are replaced by Ile92 and Phe268, respectively (Figs 4B and 8B). These water-inaccessible hydrophobic residues would also result in the lowering of NiR activity of Δ(Cyt*c*-Cup) *Br*NiR.

The superimposed structures of Δ(Cyt*c*-Cup) *Br*NiR on the core domain of 3-domain *Hd*NiR (Fig. 8C)

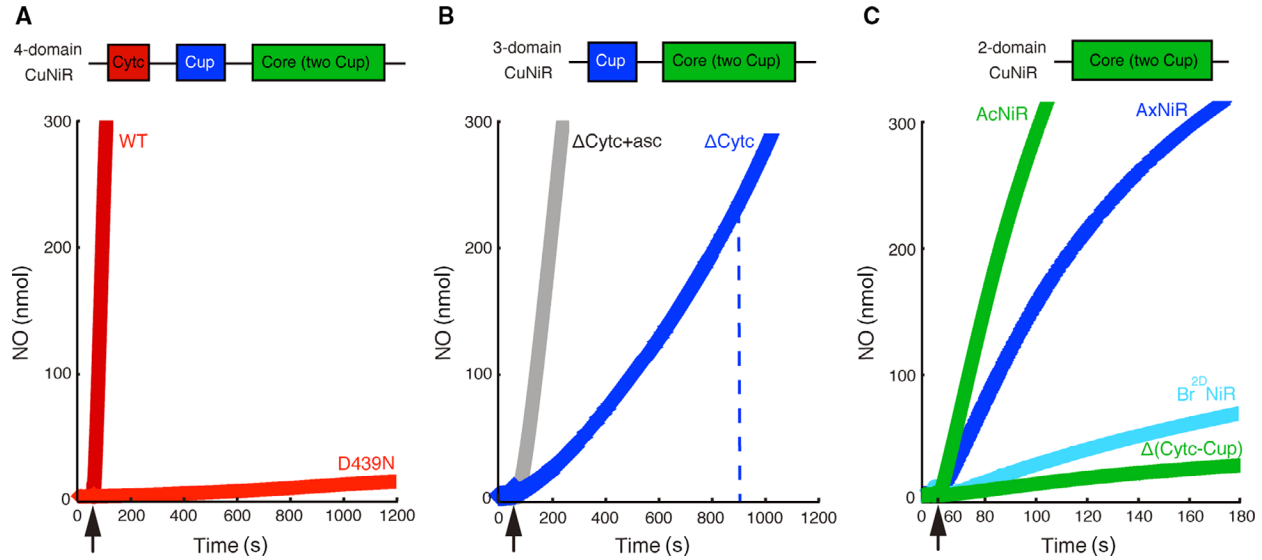

Fig. 7. NiR activity measurement profiles of the *Br*NiR variants and *Br*^{2D}NiR. Time-course NO production profiles (NO production [nmol] vs Time [s]) of (A) the wild-type (WT) *Br*NiR and site-directed mutant D439N, (B) cytochrome *c* domain-truncated mutant ΔCyt*c*, and (C) cytochrome *c*/extra cupredoxin domains-truncated mutant Δ(Cyt*c*-Cup) and *Br*^{2D}NiR/*Ax*NiR/*Ac*NiR are compared. WT/site-directed mutant, ΔCyt*c*, and Δ(Cyt*c*-Cup) are shown by red, blue, and green continuous lines, respectively. *Ax*NiR, *Br*^{2D}NiR, and *Ac*NiR are shown by blue, cyan, and green continuous lines, respectively. ΔCyt*c* *Br*NiR pre-incubated with ascorbate for 600 s before injection is shown by grey continuous line in (B). The end position of lag phase (start position of linear NO production) for ΔCyt*c* (~ 900 s) is indicated by blue broken line. Protein sample/nitrite injection positions at 60 s are indicated by black arrows. The final concentration of the enzymes in (A)/(B) and (C) is of 300 and 3 nm, respectively. The assay for the enzymes in (C) at the same concentration as used in (A)/(B) was experimentally impossible due to their much higher activity than those in (A)/(B). Specific NiR activity values [nmol s^{-1} (nmol of protein)$^{-1}$] estimated with calibration curve are summarized in Table 1.

provide insight into possible interaction between the catalytic core and tethered cupredoxin domain of 4-domain *Br*NiR (Fig. 8C). The carbonyl oxygens of Gly171 (Gly171(O))/Phe178 (Phe178(O)) and amine of Val180 (Val180(N)) are structurally conserved in Δ(Cyt*c*-Cup) *Br*NiR (green sticks in Fig. 8C). The Glu177 and Glu287, which are also structurally conserved, show a different conformation with the corresponding residues of *Hd*NiR due to the lack of the interaction with the tethered cupredoxin domain (green sticks in Fig. 8C). In addition, the homology model of the tethered cupredoxin domain of 4-domain *Br*NiR shows the structural conservation of the residues (orange sticks in Fig. 8C) paired with those of the core domain above, which predicts likely interactions of Gly171(O)-Gly(N), Phe178(O)-Ser(N), Val180(N)-Ser, Glu177-Thr(N), and Glu287-Gln(N) between the core and tethered domains in 4-domain *Br*NiR. The Thr267 of *Hd*NiR is replaced with Glu132, which could interact with Thr (Glu132-Thr) (Fig. 8C). The Ser101 of *Hd*NiR is predicted to be Ala, which is considered to make van der Waals contact with the carbonyl oxygen of Pro128 (Pro128(O)-Ala).

Structure of 2-domain *Br*^{2D}NiR

The activity of *Br*^{2D}NiR was also found to be much lower than the classical 2-domain *Ax*NiR and *Ac*NiR (Table 1). We determined the crystal structure of *Br*^{2D}NiR at high resolution of 1.47Å (Fig. 9A, Table 2). The global architecture of the monomer is similar to the classical 2-domain *Ax*NiR (PDB ID: 5ONY) [30], *Ac*NiR (PDB ID: 2BW4) [10], and *Af*NiR (PDB ID: 4YSE) [31] with r.m.s.d. values of 0.55, 0.88, and 0.58 Å (C-alphas), respectively. The biggest difference between *Br*^{2D}NiR and *Ax*NiR/*Ac*NiR is observed in the loop region (Pro132 to Met136) adjacent to the T1Cu site with a different conformation due to an additional Pro135 residue (Fig. 9C,D). Flexibility of this loop has been seen previously in an N90S *Ax*NiR mutant with a resulting loss of ~ 70% in NiR activity [32]. Though the T1Cu-to-T2Cu ET pathway *via* a Cys130-His129 bridge is completely conserved, Asn107/Gln113 for *Ax*NiR/*Ac*NiR, which forms the entrance of the major proton pathway extending towards the $Asp92_{CAT}$/$His250_{CAT}$, is replaced by Leu107 (Figs 3 and 9B). The decrease in

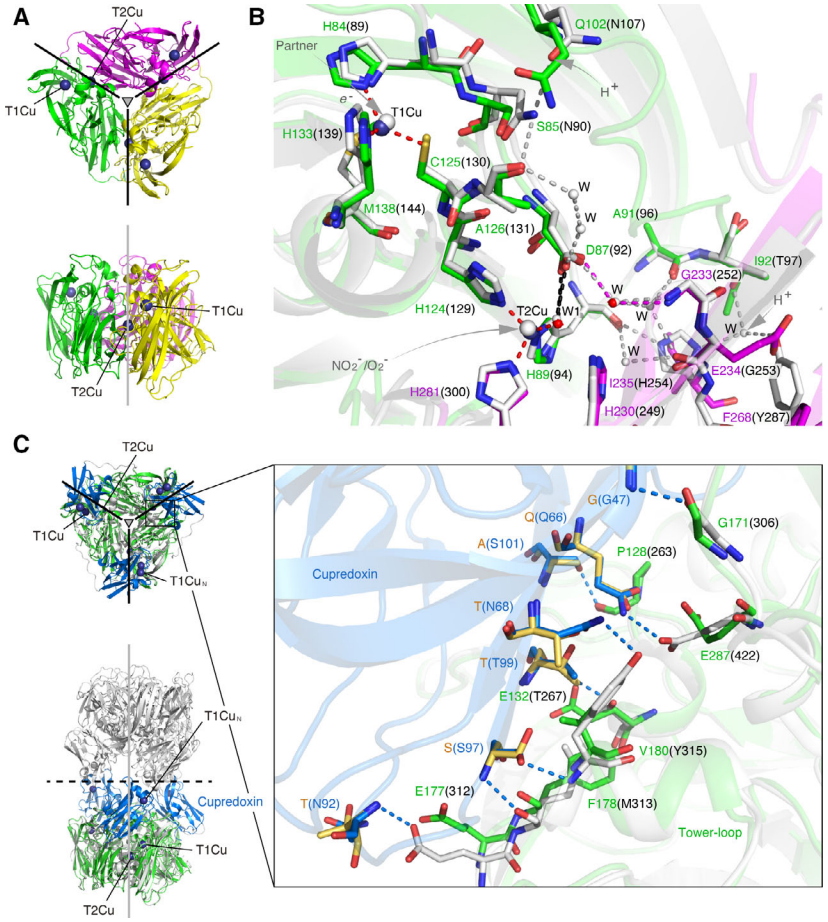

Fig. 8. Overall crystal structure of Δ(Cyt*c*-Cup) and comparison with the 2-domain *Ax*NiR/3-domain *Hd*NiR. (A) Top (upper) and side (lower) views of the trimeric core domain of 4-domain CuNiR from *Bradyrhizobium* sp. ORS 375 (Δ(Cyt*c*-Cup)). The interface between monomers is indicated by black continuous line, and threefold axis symmetry is indicated by gray triangle. (B) The Cys-His bridge and proton pathways of superimposed structures of Δ(Cyt*c*-Cup) on 2-domain *Ax*NiR being colored in green (one subunit)/magenta (neighboring subunit) and white (both of one subunit and neighboring subunit for simplicity), respectively. The T1Cu/T2Cu ions for Δ(Cyt*c*-Cup) and *Ax*NiR are shown by deep blue and light grey spheres, respectively. The water molecules (W) including the ligand water molecule (W1) to T2Cu for Δ(Cyt*c*-Cup) and *Ax*NiR are shown by red and light grey spheres, respectively. Coordination to the T1Cu/T2Cu ions is shown by red broken line. Major (N107 to D92) and minor (T97/Y287/W to D92) proton pathways of *Ax*NiR are shown by white broken lines. Major proton pathway of Δ (Cyt*c*-Cup) is invisible due to missing of the two water molecules, and minor one is partially visible and shown by magenta broken line. Numbering in the brackets is for *Ax*NiR. (C) The interaction interfaces of superimposed structures of Δ(Cyt*c*-Cup) on 3-domain CuNiR from *Hyphomicrobium denitrificans* strain A3151 (*Hd*NiR) (PDB ID: 2DV6) being colored in green and light grey, respectively. The tethered cupredoxin domain of *Hd*NiR is colored in blue. The interface between trimers of hexameric *Hd*NiR is indicated by black broken line. The T1Cu/T2Cu ions for Δ(Cyt*c*-Cup) are shown by deep blue spheres. The $T1Cu_N$ ion in the tethered cupredoxin domain of *Hd*NiR is shown by deep blue sphere. The homology model of the tethered cupredoxin domain of 4-domain *Br*NiR is superimposed on that of *Hd*NiR and shown by light orange sticks. Numbering in the brackets is for *Hd*NiR. Structural figures were prepared with PYMOL, (version 1.4 Schrödinger, LLC).

nitrite reductase activity of Br^{2D}NiR might arise from these structural differences.

The retention of activity in the *Ax*NiR mutant with mutation of Asp_{CAT} of the T2Cu site has been reported, which showed ~ 70% activity with reduced azurin as an electron donor although it was essentially inactive with artificial electron donors, suggesting a conformational change when the enzyme forms an T1Cu-to-T2Cu ET complex with its encounter partner, azurin [33]. To investigate the possibility of this kind of an interaction with encounter partner proteins, the crystallographic structure of Br^{2D}NiR was analyzed. The binding interface with partner proteins is similar to the transient *Ax*gNiR-

Table 2. Data collection and structure refinement statistics for Δ(Cyt*c*-Cup) *Br*NiR and Br^{2D}NiR.

Data collection	Δ(Cyt*c*-Cup) *Br*NiR	Br^{2D}NiR
Beamline	I24 at Diamond	I04-1 at Diamond
Wavelength (Å)	0.9686	0.9159
Space group	*I*23	$P2_13$
Unit-cell parameters		
a, *b*, *c* (Å)	125.14, 125.14, 125.14	106.93, 106.93, 106.93
α, *β*, *γ* ()	90, 90, 90	90, 90, 90
Resolution range (Å)	39.57–2.87 (3.03–2.87)[d]	106.93–1.47 (1.50–1.47)[d]
No. of reflections, total/unique	20101/7073	450989/69285
Completeness (%)	93.2 (88.8)[d]	100 (100)[d]
Redundancy	2.8 (2.6)[d]	6.5 (6.6)[d]
$<I/\sigma(I)>$	3.5 (1.7)[d]	11.3 (1.5)[d]
R_{merge}[a]	0.219 (0.481)[d]	0.081 (1.018)[d]
CC(1/2)	0.939 (0.738)[d]	0.998 (0.638)[d]
Refinement		
Resolution range (Å)	39.57–2.87	50.93–1.47
R_{work}[b]/R_{free}[c]	0.225/0.234	0.141/0.157
No. atoms		
Protein	2250	2678
Cu	2	2
Lanthanides	10	–
Cl	1	–
Pentane-1,5-diol	49	–
Sulfate	–	40
MES	–	24
Water	55	521
B-factors (Å^2)		
Protein	23.8	18.8
Cu	19.2	14.3
Lanthanides	32.0	–
Cl	26.1	–
Pentane-1,5-diol	33.1	–
Sulfate	–	43.3
MES	–	25.4
Water	18.0	35.8
R.m.s. deviations		
Bond lengths (Å)	0.002	0.013
Bond angles ()	0.653	1.667
Ramachandran plot		
Favored (%)	95.3	98.3
Allowed (%)	100	99.7
PDB ID	6THE	6THF

[a] $R_{merge} = \Sigma|I_i - I_m|/\Sigma I_i$, where I_i is the intensity of the measured reflection and I_m is the mean intensity of all symmetry related reflections.; [b] $R_{work} = \Sigma||F_{obs}|-|F_{calc}||/\Sigma|F_{obs}|$, where F_{obs} and F_{calc} are observed and calculated structure factors, respectively.

[c] $R_{free} = \Sigma_T||F_{obs}|-|F_{calc}||/\Sigma_T|F_{obs}|$, where T is a test data set of 5% of the total reflections randomly chosen and set aside prior to refinement.

[d] Numbers in parentheses represent the value for the highest resolution shell.

cytc_{551} (PDB ID: 2ZON) [7] (Fig. 9C) and *Ax*NiR-pseudoazurin complexes (PDB ID: 5B1J) [6] (Fig. 9D), suggesting similar interactions would be possible with putative cytochrome and/or cupredoxin electron donor for Br^{2D}NiR. The residues forming the hydrophobic patch, Trp139, Tyr198, and Pro88 (the latter, corresponding to Pro88 in the *Ax*gNiR-cytc_{551} complex, has been predicted to be a dominant electron acceptor from the CBC methyl group of heme [7]), adopt the same conformation (Fig. 9C). In the case of the *Ax*NiR-pseudoazurin complex, the carbonyl oxygen of Ala86 is proposed to be the key electron acceptor from His82, a ligand of the T1Cu site [6], and this oxygen of Thr86 is structurally conserved in Br^{2D}NiR (Fig. 9D). Both Met87 and Pro132 of Br^{2D}NiR have two conformations primed for conformational search for the recognition motifs of the partner proteins (Fig. 9C,D). The van der Waals contacts made by Met87, Pro88, and Pro132 of the *Ax*gNiR-cytc_{551}, corresponding to the residues above, provide a tight packing for Met135. Replacement of this methionine with a more compact side chain of Ser has been shown to decrease the second-order ET rate constant to ~ 10 times lower with cytc_{551} as a donor, indicating the importance of this packing for heme-to-T1Cu ET [7]. When compared with the *Ax*gNiR-cytc_{551}, the side chain of Met136 of the Br^{2D}NiR, which is completely conserved (Fig. 2B) and is equivalent to Met135 of *Ax*gNiR and *Ax*NiR, is found to be flipped away by 180° with the two waters bound (Fig. 9C), implying heme-to-T1Cu ET by a tight packing for this methionine in Br^{2D}NiR.

Conclusion

This study reports the discovery and characterization of a novel 4-domain CuNiR from *Bradyrhizobium* sp. ORS 375. The very low activity of the enzyme decreases when only the cytochrome domain is removed, but it increases when both tethered domains are removed. A more recent detailed work on the tethered nitrite reductase, *Rp*NiR [21], has shown that tethering does not enhance the rate of electron delivery from its tethered cytochrome *c* to the catalytic copper-containing core. The study further demonstrated that tethering communicates the redox state of the heme to the distant T2Cu center that helps initiate substrate binding for catalysis. We suggest that tethering has multiple functions that control and regulate multiple features of NiR catalysis. These include suppression of reductive enzyme inactivation, enhancing substrate binding. We suggest that tethered Cu nitrite reductases

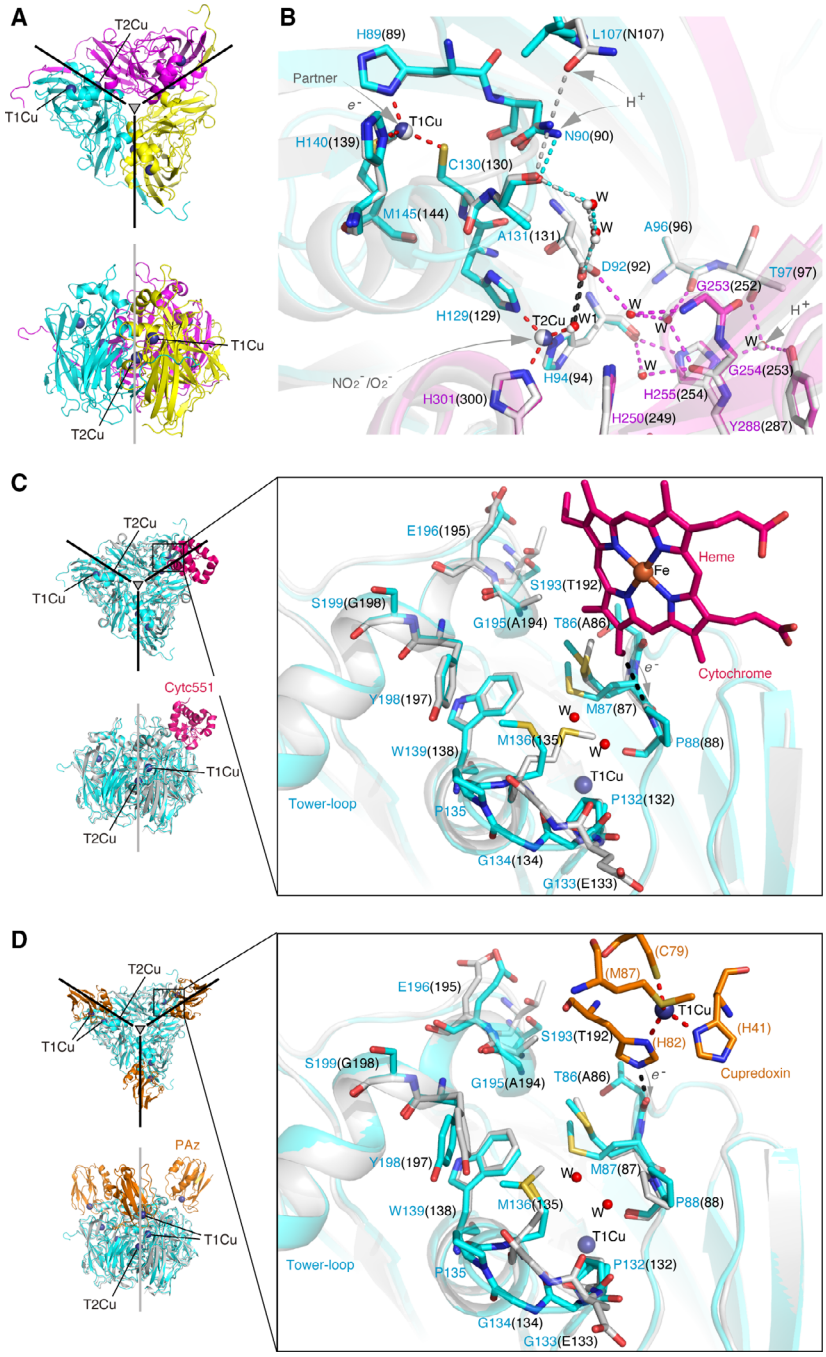

offer an exemplar system to study the role of tethering in ET, role of linker regions of cognate partners in reaching optimum geometries for multiple redox centers, coupling of redox centers involved in catalysis and communication between them that report on their redox status during catalysis. The reverse protein engineering approach utilized here with naturally evolved tethered systems illustrates a wider applicability for exploring protein–protein complexes and associated catalytic ingredients of redox enzymes including activation of catalytic site, electron transfer, control of gatekeepers, and coupling of redox centers.

Fig. 9. Overall crystal structure of Br^{2D}NiR and comparison with the classical 2-domain CuNiRs. (A) Top (upper) and side (lower) views of the trimeric 2-domain CuNiR from *Bradyrhizobium* sp. ORS 375 (Br^{2D}NiR). The interface between monomers is indicated by black continuous line, and threefold axis symmetry is indicated by gray triangle. (B) The Cys-His bridge and proton pathways of superimposed structures of Br^{2D}NiR on 2-domain *Ax*NiR (PDB ID: 5ONY) being colored in cyan (one subunit)/magenta (neighboring subunit) and white (both of one subunit and neighboring subunit for simplicity), respectively. The T1Cu/T2Cu ions for Br^{2D}NiR and *Ax*NiR are shown by deep blue and white spheres, respectively. The water molecules (W) including the ligand water molecule (W1) to T2Cu for Br^{2D}NiR and *Ax*NiR are shown by red and white spheres, respectively. Coordination to the T1Cu/T2Cu ions is shown by red broken line. Major (N90 to D92) and minor (T97/Y288/W to D92) proton pathways of Br^{2D}NiR are shown by cyan and magenta broken lines, respectively. Major (N107 to D92) proton pathway of *Ax*NiR is shown by white broken line, and minor one is completely the same with Br^{2D}NiR. Numbering in the brackets is for *Ax*NiR. (C) The binding interfaces of superimposed structures of Br^{2D}NiR on 2-domain CuNiR from *Achromobacter xylosoxidans* GIFU 1051 (*Ax*gNiR, formally known as *Alcaligenes xylosoxidans*) in transient complex with its cognate partner protein cytc_{551} (PDB ID: 2ZON) being colored in cyan and white, respectively. The cytc_{551} with heme is colored in pink. The proposed ET path from the CBC methyl group to Pro111 (4.0Å) is indicated by black broken line. (D) The binding interfaces of superimposed structures of Br^{2D}NiR on 2-domain *Ax*NiR in transient complex with its cognate partner protein pseudoazurin (PDB ID: 5B1J) being colored in cyan and white, respectively. The pseudoazurin is colored in orange. The proposed ET path from His82 ligand to carbonyl oxygen of Thr109 (2.5Å) is indicated by black broken line. The T1Cu/T2Cu ions for Br^{2D}NiR are shown by deep blue spheres. The heme Fe and T1Cu ions for cytc_{551} and pseudoazurin are shown by orange and deep blue spheres, respectively. The water molecule (W) for Br^{2D}NiR is shown by red spheres. Coordination to the T1Cu ion for pseudoazurin is shown by red broken line. Numbering in the brackets is for *Ax*gNiR-cytc_{551}/*Ax*NiR-pseudoazurin complex. Structural figures were prepared with PYMOL, version 1.4 (Schrödinger, LLC).

Materials and Methods

Primary structure alignment

Multiple sequence alignment was performed with ClustalW [34], and the aligned sequences were illustrated using ESPript [35]. Amino-acid sequence identity was estimated with BLAST by performing one-to-one pairwise analysis [36]. Primary sequence information was obtained from the Universal Protein Resource (UniProt) (http://www.uniprot.org).

Preparation of 4-domain *Br*NiR variants

The wild-type (WT) *Br*NiR, domain-truncated (ΔCyt*c* and Δ(Cyt*c*-Cup)), and site-directed (D439N) *Br*NiR mutant genes were ordered from GenScript (Piscataway, USA) with the NCBI reference coding: WP_009028608.1. The N-terminal signal peptide predicted by Signal-3L 2.0 [37] was removed. The gene with TEV cleavage site was cloned into pET-26b(+) (Novagen, Darmstadt, Germany) between NdeI and XhoI sites. The resultant plasmid was verified by DNA sequencing.

Escherichia coli host strain BL21(DE3) cell (New England BioLabs Inc.) was transformed with the plasmid and chloramphenicol-resistant pEC86 encoding the cytochrome *c* maturation genes *ccm*ABCDEFGH for overexpression of WT and D439N. A single colony was grown in 50 mL of Luria–Bertani (LB) medium supplemented with 50 μg/mL kanamycin and 34 μg/mL chloramphenicol and incubated at 37°C for 16 h at 240 rpm. Five mL of culture was inoculated into 500 mL of LB medium in baffled flask supplemented with the same concentration of kanamycin and chloramphenicol and incubated at 37°C at 180 rpm until OD_{600nm} reached ~ 0.6. Subsequently, a final concentration of 1.0 mM $CuSO_4$, 50 μg/mL hemin, and 0.5 mM isopropyl β-D-1-thiogalactopyranoside (IPTG) were added and overexpression was induced at 18°C for 16 h at 120 rpm. The cells were harvested by centrifugation (4,690 g, 45 min, 4°C). The pellet was washed with 50 mL of phosphate-buffered saline (PBS) pH 7.4 and harvested by centrifugation (3,140 g, 30 min, 4°C).

The cells were suspended in 50 mL of lysis buffer 100 mM Tris/HCl (pH 8.0), 500 mM NaCl, and 10 mM imidazole containing protease inhibitor tablet (Roche) for 1 L culture. After lysozyme was added to a final concentration of 0.5 mg/mL, the suspension solution was incubated on ice for 20 min. The cells were disrupted by sonication on ice. The cell debris was removed by centrifugation (29 900 ***g***, 45 min, 4°C). The supernatant was filtered and applied to a 5 mL of His-tag affinity column HisTrap™ HP (GE healthcare, Buckinghamshire, UK) equilibrated with the lysis buffer. The resin was washed with the same buffer, and protein was eluted with 10 mL of elution buffer 100 mM Tris/HCl (pH 8.0), 500 mM NaCl, and 250 mM imidazole. The elution solution was dialyzed at 4°C for 24 h against size exclusion chromatography (SEC) buffer 100 mM Tris/HCl (pH 8.0), 500 mM NaCl, and 10% (v/v) glycerol. After dialysis, a final concentration of 2 mM DTT was added and protein was incubated with TEV protease (50 : 1) at 4°C for 16 h to remove the 6xHis-tag. The protein solution was concentrated and applied on SEC column HiLoad Superdex 200 16/600 pg (GE Healthcare, Buckinghamshire, UK) equilibrium with SEC buffer. The protein was eluted at a flow rate of 1.0 mL/min. The elution fractions were dialyzed at 4°C for 16 h against Cu-loading buffer, SEC buffer with 0.1 mM $CuSO_4$, to reconstitute T2Cu site. After dialysis, the protein solution was concentrated and applied again on the same SEC column equilibrated with SEC buffer. The protein was eluted at a flow rate of 1.0 mL/min. The elution fractions were concentrated and

stored at −80°C. All chromatography steps were performed at 4°C. The ΔCyt*c* and Δ(Cyt*c*-Cup) samples were prepared with the method used for WT with some modifications (modified parts are underlined); *E. coli* was transformed with the ordered single plasmid without pEC86, so that chloramphenicol and hemin were not used. Overexpression was induced at 180 rpm using an un-baffled flask. The elution fractions in 2nd SEC were dialyzed at 4°C for 16 h against Cu-loading buffer, SEC buffer with 1.0 mM $CuSO_4$, to reconstitute T2Cu site.

Preparation of 3-domain *Hd*NiR

The *Hd*NiR gene was ordered from Invitrogen (Carlsbad, USA) with GenBank coding: BAC00912.1. The signal peptide sequence at N terminus, predicted by signal peptide prediction server Signal-3L 2.0 [37], was removed from the ordered gene. The gene with TEV cleavage site was cloned into pETM-11 (EMBL, Heidelberg, Germany) between NcoI and XhoI. The resultant plasmid was verified by DNA sequencing.

Escherichia coli host strain BL21 cell (New England BioLabs Inc.) was transformed with the plasmid. A single isolated colony was grown in 5 mL culture of LB medium supplemented with 50 μg/mL kanamycin and incubated at 37°C for 3 h with shaking at 190 rpm. This culture was inoculated into 200 mL of LB medium (1 : 40 ratio) for 16 h. Five mL of culture was inoculated into 500 mL LB medium (1 : 100 ratio) supplemented with the same concentration of kanamycin and incubated at 30°C with shaking at 190 rpm until OD_{600nm} reaches ~ 0.6. The temperature of culture solution was dropped to 20°C. Subsequently, a final concentration of 0.1 mM $CuSO_4$ and 0.3 mM IPTG was added and overexpression was induced at 20°C for 16 h with shaking at 190 rpm. The cells were harvested by centrifugation (2,000 g, 10 min, 4°C).

The cells were suspended in lysis buffer 40 mM MOPS (pH 7.8), 150 mM NaCl containing protease inhibitor tablet (Roche), DNase, and 5 mM $MgCl_2$. The cells were disrupted by sonication on ice. The cell debris was removed by centrifugation (32 800 ***g***, 45 min, 4°C). The supernatant was applied to a 5 mL of His-tag affinity column HisTrap™ HP (GE Healthcare, Buckinghamshire, UK) equilibrated with the lysis buffer. The resin was washed with the wash buffer, lysis buffer with 50 mM imidazole, and protein was eluted with enough volume of elution buffer, lysis buffer with 250 mM imidazole. The elution solution was buffer-exchanged into 50 mM Tris/HCl pH 7.8, 200 mM NaCl, and 1 mM DTT. Protein was incubated with TEV protease (20 : 1) at room temperature for 12 h on a roller to remove the 6xHis-tag. The protein solution was buffer-exchanged into 50 mM Tris/HCl pH7.8, 200 mM NaCl to remove cleaved 6xHis peptide and DTT. A final concentration of 0.3 mM $CuSO_4$ was added to reconstitute T2Cu site. The protein solution was buffer-exchanged into the same buffer to remove remaining $CuSO_4$ and then concentrated and stored at −80°C. The first His-tag affinity purification steps were performed at 4°C, and the latter steps were done at room temperature.

Preparation of 2-domain *Br*^{2D}NiR, *Ax*NiR, and *Ac*NiR

The *Br*^{2D}NiR gene was ordered from GenScript with the NCBI reference coding: WP_009030123.1. The N-terminal signal peptide predicted by Signal-3L 2.0 [37] was removed from the ordered gene. The gene with TEV cleavage site was cloned into pET-26b(+) between NdeI and XhoI sites. The resultant plasmid was verified by DNA sequencing.

Escherichia coli host strain BL21(DE3) cell (New England BioLabs Inc.) was transformed with the plasmid. A single colony was grown in 50 mL of Luria–Bertani (LB) medium supplemented with 50 μg/mL kanamycin and incubated at 37°C for 16 h at 240 rpm. Five mL of culture was inoculated into 500 mL of LB medium supplemented with the same concentration of kanamycin and incubated at 37°C at 180 rpm until OD_{600nm} reached ~ 0.6. Subsequently, a final concentration of 1.0 mM $CuSO_4$ and 0.5 mM isopropyl β-D-1-thiogalactopyranoside (IPTG) was added and overexpression was induced at 18°C for 16 h at 180 rpm. The cells were harvested by centrifugation (4,690 g, 45 min, 4°C). The pellet was washed with 50 mL of phosphate-buffered saline (PBS) pH 7.4 and harvested by centrifugation (3,140 g, 30 min, 4°C).

The cells were suspended in 50 mL of lysis buffer 100 mM Tris/HCl (pH 8.0), 500 mM NaCl containing protease inhibitor tablet (Roche) for 1 L culture. After lysozyme was added to a final concentration of 0.5 mg/mL, the suspension solution was incubated on ice for 20 min. The cells were disrupted by sonication on ice. The cell debris was removed by centrifugation (29 900 ***g***, 45 min, 4°C). The supernatant was filtered and dialyzed at 4°C for 16 h against the lysis buffer with 0.1 mM $CuSO_4$. The precipitate was removed by centrifugation (4,500 g, 10 min, 4°C). The supernatant was filtrated and applied to a 5 mL of His-tag affinity column HisTrap™ HP (GE Healthcare, Buckinghamshire, UK) equilibrated with the lysis buffer with 10 mM imidazole. The resin was washed with the same buffer, and protein was eluted with 10 mL of elution buffer 100 mM Tris/HCl (pH 8.0), 500 mM NaCl, and 250 mM imidazole. The elution solution was dialyzed at 4°C for 24 h against size exclusion chromatography (SEC) buffer 100 mM Tris/HCl (pH 8.0), 500 mM NaCl, and 10% (v/v) glycerol. After dialysis, a final concentration of 2 mM DTT was added and protein was incubated with TEV protease (50 : 1) at 4°C for 16 h to remove the 6xHis-tag. The protein solution was concentrated and applied on SEC column HiLoad Superdex 200 16/600 pg (GE Healthcare, Buckinghamshire, UK) equilibrium with SEC buffer. The protein was eluted at a flow rate of 1.0 mL/min. The elution fractions were concentrated and dialyzed at 4°C for 16 h

against Cu-loading buffer, SEC buffer with 1.0 mM $CuSO_4$, to reconstitute T2Cu site. After dialysis, the protein solution was concentrated and stored at −80°C. All chromatography steps were performed at 4°C.

*Ax*NiR was prepared with the methods previously reported [26]. *Ac*NiR was prepared with the methods previously reported [38] with some modifications; a single colony was grown in LB medium supplemented with 30 μg/mL kanamycin. $CuSO_4$ (1 mM) was added and overexpression was induced with 2.0 mM IPTG. The induction was continued for 24 h. The harvested cells were resuspended in 20 mM Tris/HCl (pH 7.5) and 0.1 mg/mL lysozyme before being disrupted by sonication. The lysate was collected by centrifugation (36 900 ***g***, 45 min, 4°C) and dialyzed against 20 mM Tris/HCl buffer (pH 7.5) and 2 mM $CuSO_4$, followed by dialysis against water after which the lysate turned from pale yellow to bright green. After the lysate was loaded onto a diethylaminoethyl (DEAE)-cellulose column (Sigma-Aldrich, St. Louis, USA), the column was washed with 20 mM Tris/HCl (pH 7.5) followed by 100 mM Tris/HCl (pH 7.5). The protein was eluted using a NaCl gradient from 100 to 250 mM in 20 mM Tris/HCl (pH 7.5). After further purification by ammonium sulfate precipitation, the protein solution was buffer-changed into 10 mM HEPES-OH (pH 6.5).

UV-visible absorption spectrum measurement

UV-visible absorption spectrum was recorded at room temperature on Cray 300 Bio UV-visible spectrophotometer (Varian, Palo Alto, USA). The oxidized WT *Br*NiR sample was prepared at 1.0 mg/mL in SEC buffer, and the spectrum was recorded. The reduced WT *Br*NiR sample was prepared by adding 100-fold molar excess of sodium dithionite to this solution under anaerobic condition, and the spectrum was recorded. The oxidized ΔCyt*c*, Δ(Cyt*c*-Cup), and Br^{2D}NiR samples were prepared at 1.0 mg/mL in the same buffer, and the spectra were recorded. The oxidized *Hd*NiR/*Ax*NiR/*Ac*NiR samples were prepared at 1.0 mg/mL in 10 mM Tris/HCl (pH 7.8), 200 mM NaCl/10 mM Tris/HCl (pH 7.5)/10 mM HEPES (pH 6.5), respectively, and the spectra were recorded.

Oligomeric state analysis

Molecular mass of the *Br*NiR variants was estimated by comparison with retention volumes of marker proteins (GE Healthcare, Buckinghamshire, UK). The marker proteins, blue dextran (2,000 kDa), thyroglobulin (669 kDa), ferritin (440 kDa), aldolase (158 kDa), conalbumin (75 kDa), and ovalbumin (44 kDa), dissolved in SEC buffer 100 mM Tris/HCl (pH 8.0), 500 mM NaCl, and 10% v/v glycerol, were applied on 120 mL of SEC column HiLoad Superdex 200 16/600 pg (GE Healthcare, Buckinghamshire, UK) equilibrium with SEC buffer and eluted at a flow of 1.0 mL/min. Calibration curve (K_{av} value vs log[Mw] (Mw: molecular weight)) for these marker proteins was made. The K_{av} value is defined with the equation $K_{av} = (V_e - V_o)/(V_c - V_o)$, where V_e, V_o, and V_c are the elution, column void, and geometric column volumes, respectively. The molecular mass of the *Br*NiR variants was estimated with their V_e values using the calibration curve.

NiR activity measurement

NiR activity was assessed under the anaerobic condition using an NO detectable ISO-NOP electrode (World Precision Instruments, Sarasota, USA). The 3 mL of assay mixture 'initial pH 6.5' contained nitrogen saturated 50 mM HEPES buffer (pH 6.5), 8.0 mM sodium ascorbate, 80 μM phenazine methosulfate (PMS), and 8.0 mM sodium nitrite was prepared in the vessel under the anaerobic condition. The electrode was inserted into the mixture, and baseline voltage was confirmed to be constant for 1 min to confirm non-enzymatic NO formation. The reaction was started by the addition of tiny volume of sample at a final concentration of 300 nM for WT *Br*NiR, D439N *Br*NiR, ΔCyt*c* *Br*NiR, and *Hd*NiR and 3 nM for Δ(Cyt*c*-Cup) *Br*NiR, Br^{2D}NiR, *Ax*NiR, and *Ac*NiR, respectively, and time-course NO production (Voltage [V] vs Time [sec]) was monitored. Activity value [nmol sec^{-1} (nmol of protein)$^{-1}$] for linear slope in each measurement was estimated using the calibration curve (Voltage [V] vs NO production [nmol]), which was experimentally determined.

Structure determination of 2-domain Δ(Cyt*c*-Cup) *Br*NiR

The Δ(Cyt*c*-Cup) sample in 100 mM Tris/HCl (pH 8.0), 500 mM NaCl, and 10% (v/v) glycerol was buffer-exchanged into 20 mM Tris/HCl (pH 8.0) and concentrated to 10 mg/mL. Protein was crystallized by sitting drop vapor diffusion method: 0.1 μL of sample solution was mixed with an equal volume of crystallization reagent 10% (w/v) PEG 8,000, 20% (v/v) 1,5-pentanediol, 0.1 M MOPSO/Bis-Tris (pH 6.5), 0.005 M Yttrium (III) chloride hexahydrate, 0.005 M Erbium (III) chloride hexahydrate, 0.005 M Terbium (III) chloride hexahydrate, and 0.005 M Ytterbium (III) chloride hexahydrate, and equilibrated over 80 μL of the crystallization reagent at room temperature. The crystal was flash-cooled in liquid nitrogen. Diffraction data set was collected at the I24 beamline, Diamond Light Source, UK, at 100 K using Pilatus3 6M detector. The diffraction images were processed with xia2 [39] using DIALS [40] and merged with AIMLESS [41]. The initial model was obtained by molecular replacement with MOLREP [42] using the structure of core domain of

*Hd*NiR monomer (PDB ID: 2DV6). The model was manually rebuilt with Coot [43] and refined with REFMAC5 [44] in CCP4 [45]. The quality of the final model was accessed with MolProbity [46]. Data collection and structure refinement statistics are summarized in Table 2. Structural figures were prepared with PYMOL (Version 1.4 Schrödinger, LLC).

Structure determination of 2-domain *Br*^{2D}NiR

The *Br*^{2D}NiR sample in 100 mM Tris/HCl (pH 8.0), 500 mM NaCl, and 10% (v/v) glycerol was buffer-exchanged into 10 mM HEPES (pH 6.5) and concentrated to 10 mg/mL. Protein was crystallized by hanging drop vapor diffusion method: 1 μL of sample solution was mixed with an equal volume of crystallization reagent 1.2 M ammonium sulfate, 0.05 M MES (pH 6.0), and equilibrated over 200 μL of the crystallization reagent at room temperature. The crystal was transferred in 3.2 M ammonium sulfate and 0.1 M MES (pH 6.0) and flash-cooled in liquid nitrogen. Diffraction data set was collected at the I04-1 beamline, Diamond Light Source, UK, at 100 K using Pilatus 6M-F detector. The diffraction images were processed with xia2 [39] using DIALS [40]. The initial model was obtained by molecular replacement with MOLREP [42] using the structure of *Ac*NiR monomer (PDB ID: 5I6K). The model was automatically rebuilt with ARP/wARP [47] followed with manual rebuilding with Coot [43] and refined with REFMAC5 [44] in CCP4 [45]. The quality of the final model was accessed with MolProbity [46]. Data collection and structure refinement statistics are summarized in Table 2. Structural figures were prepared with PYMOL, version 1.4 (Schrödinger, LLC).

3D structure alignment and prediction

3D structure alignment and homology modeling were performed with TM-align [48] and I-TASSER [49], respectively.

Acknowledgements

This work was supported by the Biotechnology and Biological Sciences Research Council, UK (Grant number BB/N013972/1 to SSH/SVA). S.S.H. was the recipient of a PVE award funded by CNPq (grant number 407438/2013-0), which also funded T.F.W. The authors would like to thank Diamond Light Source, UK (MX15991 BAG), for synchrotron access.

Author contributions

RRE, SVA, RCG, and SSH conceived and designed the project. DS and TFW performed the experiments. DS, TFW, RRE, SVA, RCG, and SSH analyzed the data. DS, RRE, SVA, RCG, and SSH wrote the paper.

Conflict of interest

The authors declare no conflict of interest.

References

1 Moser CM, Keske M, Warnke K, Farid RS & Dutton PL (1992) Nature of biological electron transfer. *Nature* **355**, 796–802.
2 Nie Y, Viola C, Bieniossek C, Trowitzsch S, Vijayachandran LS, Chaillet M, Garzoni F & Berger I (2009) Getting a grip on complexes. *Curr Genomics* **10**, 558–572.
3 Zumft WG (1997) Cell biology and molecular basis of denitrification. *Microbiol Mol Biol Rev* **61**, 533–616.
4 Ravishankara AR, Daniel JS & Portmann RW (2009) Nitrous oxide (N_2O): the dominant ozone-depleting substance emitted in the 21st century. *Science* **326**, 123–125.
5 Decleyre H, Heylen K, Tytgat B & Willems A (2016) Highly diverse nirK genes comprise two major clades that harbor ammonium producing denitrifiers. *BMC Genom* **17**, 155–167.
6 Nojiri M (2016) Structure and function of copper nitrite reductase. In Metalloenzymes in denitrification: applications and environmental impacts (Moura I, Moura JJG, Pauleta SR & Maia LB, eds), pp. 91–113. The Royal Society of Chemistry, Cambridge, UK.
7 Nojiri M, Koteishi H, Nakagami T, Nakagami T, Kobayashi K, Inoue T, Yamaguchi K & Suzuki S (2009) Structural basis of inter-protein electron transfer for nitrite reduction in denitrification. *Nature* **462**, 117–120.
8 Godden JW, Turley S, Teller DC, Adman E, Liu M, Payne W & LeGall J (1991) The 2.3 angstrom X-ray structure of nitrite reductase from *Achromobacter cycloclastes*. *Science* **253**, 438–442.
9 Dodd FE, Van Beeumen J, Eady RR & Hasnain SS (1998) X-ray structure of a blue-copper nitrite reductase in two crystal forms. The nature of the copper sites, mode of substrate binding and recognition by redox partner. *J Mol Biol* **282**, 369–382.
10 Antonyuk SV, Strange RW, Sawers G, Eady RR & Hasnain SS (2005) Atomic resolution structures of resting-state, substrate- and product-complexed Cu-nitrite reductase provide insight into catalytic mechanism. *Proc Natl Acad Sci USA* **102**, 12041–12046.
11 Boulanger MJ, Kukimoto M, Nishiyama M, Horinouchi S & Murphy ME (2000) Catalytic roles for two water bridged residues (Asp98 and His255) in the

active site of copper-containing nitrite reductase. *J Biol Chem* **275**, 23957–23964.
12 Tocheva EI, Rosell FI, Mauk AG & Murphy ME (2004) Side-on copper-nitrosyl coordination by nitrite reductase. *Science* **304**, 867–870.
13 Kataoka K, Furusawa H, Takagi K, Yamaguchi K & Suzuki S (2000) Functional analysis of conserved aspartate and histidine residues located around the type 2 copper site of copper-containing nitrite reductase. *J Biochem* **127**, 345–350.
14 Nojiri M, Xie Y, Inoue T, Yamamoto T, Matsumura H, Kataoka K, Deligeer, Yamaguchi K, Kai Y & Suzuki S (2007) Structure and function of a hexameric copper-containing nitrite reductase. *Proc Natl Acad Sci USA* **104**, 4315–4320.
15 Antonyuk SV, Han C, Eady RR & Hasnain SS (2013) Structures of protein-protein complexes involved in electron transfer. *Nature* **496**, 123–126.
16 Opperman DJ, Murgida DH, Dalosto SD, Brondino CD & Ferroni FM (2019) A three-domain copper-nitrite reductase with a unique sensing loop. *IUCrJ* **6**, 248–258.
17 Ellis MJ, Grossmann JG, Eady RR & Hasnain SS (2007) Genomic analysis reveals widespread occurrence of new classes of copper nitrite reductases. *J Biol Inorg Chem* **12**, 1119–1127.
18 Tsuda A, Ishikawa R, Koteishi H, Tange K, Fukuda Y, Kobayashi K, Inoue T & Nojiri M (2013) Structural and mechanistic insights into the electron flow through protein for cytochrome c-tethering copper nitrite reductase. *J Biochem* **154**, 51–60.
19 Chen PF, Tsai AL, Berka V & Wu KK (1996) Endothelial nitric-oxide synthase. Evidence for bidomain structure and successful reconstitution of catalytic activity from two separate domains generated by a baculovirus expression system. *J Biol Chem* **271**, 14631–14635.
20 Munro AW, Lindsay JG, Coggins JR, Kelly SM & Price NC (1994) Structural and enzymological analysis of the interaction of isolated domains of cytochrome P-450 BM3. *FEBS Lett* **343**, 70–74.
21 Hedison TM, Shenoy RT, Iorgu AI, Heyes DJ, Fisher K, Wright GSA, Hay S, Eady RR, Antonyuk SV, Hasnain SS *et al.* (2019) Unexpected roles of a tether harboring a tyrosine gatekeeper residue in modular nitrite reductase catalysis. *ACS Catal* **9**, 6087–6099.
22 MoloubaF, Lorquin J, WillemsA, Hoste B, Giraud E, Dreyfus B, Gillis M, de Lajudie P & Masson-Boivin C (1999) Photosynthetic bradyrhizobia from *Aeschynomene* spp. are specific to stem-nodulated species and form a separate 16S ribosomal DNA restriction fragment length polymorphism group. *Appl Environ Microbiol* **65**, 3084–3094.
23 Hira D, Toh H, Migita CT, Okubo H, Nishiyama T, Hattori M, Furukawa K & Fujii T (2012) Anammox organism KSU-1 expresses a NirK-type copper-containing nitrite reductase instead of a NirS-type with cytochrome cd_1. *FEBS Lett* **586**, 1658–1663.
24 Lawton TJ, Bowen KE, Sayavedra-Soto LA, Arp DJ & Rosenzweig AC (2013) Characterization of a nitrite reductase involved in nitrifier denitrification. *J Biol Chem* **288**, 25575–25583.
25 Basaglia M, Toffanin A, Baldan E, Bottegal M, Shapleigh JP & Casella S (2007) Selenite-reducing capacity of the copper containing nitrite reductase of *Rhizobium sullae*. *FEMS Microbiol Lett* **269**, 124–130.
26 Ellis MJ, Dodd FE, Sawers RG, Eady RR & Hasnain SS (2003) Atomic resolution structures of native copper nitrite reductase from *Alcaligenes xylosoxidans* and the active site mutant Asp92Glu. *J Mol Biol* **328**, 429–438.
27 Ghosh S, Dey A, Sun Y, Scholes CP & Solomon EI (2009) Spectroscopic and computational studies of nitrite reductase: proton induced electron transfer and backbonding contributions to reactivity. *J Am Chem Soc* **131**, 277–288.
28 Boulanger MJ & Murphy MEP (2002) Crystal structure of the soluble domain of the major anaerobically induced outer membrane protein (AniA) from pathogenic *Neisseria*: a new class of copper-containing nitrite reductases. *J Mol Biol* **315**, 1111–1127.
29 Yamaguchi K, Kobayashi M, Kataoka K & Suzuki S (2003) Characterization of two Cu-containing protein fragments obtained by limited proteolysis of *Hyphomicrobium denitrificans* A3151 nitrite reductase. *Biochem Biophys Res Commun* **300**, 36–40.
30 Fukuda Y, Tse KM, Nakane T, Nakatsu T, Suzuki M, Sugahara M, Inoue S, Masuda T, Yumoto F, Matsugaki N *et al.* (2016) Redox-coupled proton transfer mechanism in nitrite reductase revealed by femtosecond crystallography. *Proc. Natl. Acad. Sci. U.S.A.* **113**, 2928–2933.
31 Leferink NGH, Han C, Antonyuk SV, Heyes DJ, Rigby SEJ, Hough MA, Eady RR, Scrutton NS & Hasnain SS (2011) Proton-coupled electron transfer in the catalytic cycle of *Alcaligenes xylosoxidans* copper-dependent nitrite reductase. *Biochemistry* **50**, 4121–4131.
32 Halsted TP, Yamashita K, Hirata K, Ago H, Ueno G, Tosha T, Eady RR, Antonyuk SV, Yamamoto M & Hasnain SS (2018) An unprecedented dioxygen species revealed by serial femtosecond rotation crystallography in copper nitrite reductase. *IUCrJ* **5**, 22–31.
33 Prudêncio M, Eady RR & Sawers G (2001) Catalytic and spectroscopic analysis of blue copper-containing nitrite reductase mutants altered in the environment of the type 3 copper centre: implications for substrate interaction. *Biochem. J.* **353**, 259–266.

34 Thompson JD, Higgins DG & Gibson TJ (1994) CLUSTAL W: improving the sensitivity of progressive multiple sequence alignment through sequence weighting, position-specific gap penalties and weight matrix choice. *Nucleic Acids Res* **22**, 4673–4680.
35 Gouet P, Courcelle E, Stuart DI & Metoz F (1999) ESPript: analysis of multiple sequence alignments in PostScript. *Bioinformatics* **15**, 305–308.
36 Altschul SF, Madden TL, Schäffer AA, Zhang J, Zhang Z, Miller W & Lipman DJ (1997) Gapped BLAST and PSI-BLAST: a new generation of protein database search programs. *Nucleic Acids Res* **25**, 3389–3402.
37 Zhang YZ & Shen HB (2017) Signal-3L 2.0: A hierarchical mixture model for enhancing protein signal peptide prediction by incorporating residue-domain cross-level features. *J Chem Inf Model* **57**, 988–999.
38 Horrell S, Antonyuk SV, Eady RR, Hasnain SS, Hough MA & Strange RW (2016) Serial crystallography captures enzyme catalysis in copper nitrite reductase at atomic resolution from one crystal. *IUCrJ* **3**, 271–281.
39 Winter G (2010) xia2: an expert system for macromolecular crystallography data reduction. *J Appl Cryst* **43**, 186–190.
40 Winter G, Waterman DG, Parkhurst JM, Brewster AS, Gildea RJ, Gerstel M, Fuentes-Montero L, Vollmar M, Michels-Clark T, Young ID *et al.* (2018) DIALS: implementation and evaluation of a new integration package. *Acta Cryst D* **74**, 85–97.
41 Evans PR & Murshudov GN (2013) How good are my data and what is the resolution? *Acta Cryst D* **69**, 1204–1214.
42 Vagin A & Teplyakov (2010) A molecular replacement with MOLREP. *Acta Cryst D* **66**, 22–25.
43 Emsley P, Lohkamp B, Scott WG & Cowtan K (2010) Features and development of Coot. *Acta Cryst D* **66**, 486–501.
44 Murshudov GN, Skubák P, Lebedev AA *et al.* (2011) REFMAC5 for the refinement of macromolecular crystal structures. *Acta Cryst D* **67**, 355–367.
45 Winn MD, Ballard CC, Cowtan KD, Dodson EJ, Emsley P, Evans PR, Keegan RM, Krissinel EB, Leslie AGW, McCoy A *et al.* (2011) Overview of the CCP4 suite and current developments. *Acta Cryst D* **67**, 235–242.
46 Chen VB, Arendall WB 3rd, Headd JJ, Keedy DA, Immormino RM, Kapral GJ, Murray LW, Richardson JS & Richardson DC (2010) MolProbity: all-atom structure validation for macromolecular crystallography. *Acta Cryst D* **66**, 12–21.
47 Langer GG, Hazledine S, Wiegels T, Carolan C & Lamzin VS (2013) Visual automated macromolecular model building. *Acta Cryst D* **69**, 635–641.
48 Zhang Y & Skolnick J (2005) TM-align: a protein structure alignment algorithm based on the TM-score. *Nucleic Acids Res* **33**, 2302–2309.
49 Yang J & Zhang Y (2015) I-TASSER server: new development for protein structure and function predictions. *Nucleic Acids Res* **43**, W174–W181.